LBL-13423

Lawrence Berkeley Laboratory
UNIVERSITY OF CALIFORNIA

Materials & Molecular Research Division

RECEIVED
LAWRENCE
BERKELEY LABORATORY

FEB 10 1982

LIBRARY AND
DOCUMENTS SECTION

MICROFRACTURE IN BRITTLE SOLIDS

Yen Fu
(M.S. thesis)

October 1981

TWO-WEEK LOAN COPY

This is a Library Circulating Copy which may be borrowed for two weeks. For a personal retention copy, call Tech. Info. Division, Ext. 6782

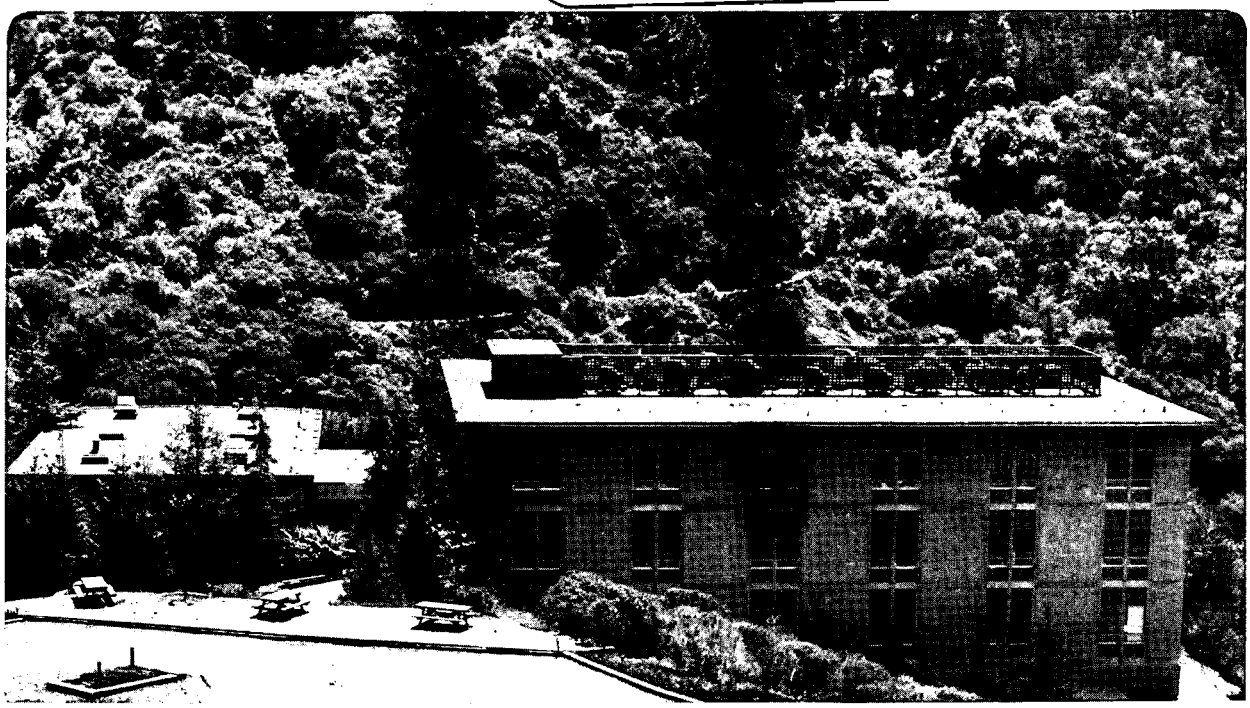

Prepared for the U.S. Department of Energy under Contract W-7405-ENG-48

LBL-13423 c.2

DISCLAIMER

This document was prepared as an account of work sponsored by the United States Government. While this document is believed to contain correct information, neither the United States Government nor any agency thereof, nor the Regents of the University of California, nor any of their employees, makes any warranty, express or implied, or assumes any legal responsibility for the accuracy, completeness, or usefulness of any information, apparatus, product, or process disclosed, or represents that its use would not infringe privately owned rights. Reference herein to any specific commercial product, process, or service by its trade name, trademark, manufacturer, or otherwise, does not necessarily constitute or imply its endorsement, recommendation, or favoring by the United States Government or any agency thereof, or the Regents of the University of California. The views and opinions of authors expressed herein do not necessarily state or reflect those of the United States Government or any agency thereof or the Regents of the University of California.

LBL-13423

MICROFRACTURE IN BRITTLE SOLIDS

by

Yen Fu
M. S. Thesis

Materials and Molecular Research Division
Lawrence Berkeley Laboratory
and
Department of Materials Science and Mineral Engineering
University of California
Berkeley, CA 94720

This work was supported by the Director, Office of Energy Research, Office of Basic Energy Sciences, Materials Science Division of the U. S. Department of Energy under Contract No. W-7405-ENG-48.

TABLE OF CONTENTS

	Page
LIST OF SYMBOLS	v
ABSTRACT	vii
1. INTRODUCTION	1
2. GENERAL METHOD OF SOLUTION	4
3. MICROFRACTURE INDUCED BY PHASE TRANSFORMATION IN ZrO_2	7
3.1 Observations	7
3.2 Stress Analysis	9
3.3 The Stress Intensity Factor	12
3.4 Analysis of Microfracture	14
3.5 Discussion	17
4. MICROCRACKING IN SINGLE PHASE POLYCRYSTALS	18
4.1 Observations	18
4.2 Stress Analysis	20
4.3 The Critical Microcracking Condition	24
5. CONCLUSION	28
ACKNOWLEDGMENT	30
APPENDIX 1	31
APPENDIX 2	36
REFERENCES	40
TABLE	42
FIGURE CAPTIONS	43
FIGURES	45

List of Symbols

σ_{ij}	stress component
σ^T_{ij}	transformation stress
σ^T	transformation stress in maximum contraction direction
σ^T_s	transformation stress in minimum contraction direction
σ^c_{ij}	constrained stress
ε^T_{ij}	transformation strain
C_{ijk}	element of compliance tensor
C	crack size
P	surface traction
S	surface area
r, θ	polar coordinate
K	stress intensity factor
E	Young's modulus
ν	Poisson ratio
μ	shear modulus
γ_T	transformation shear strain of ZrO_2
d	width of ZrO_2 variant
b	Burgers vector
c	fracture energy
T_g	freezing temperature
ΔT	temperature range
$\dot{T}$	freezing rate

$\gamma_{g.b.}$	grain boundary energy
	grain size
c	critical grain size (of spontaneous microfracture)
α	coefficient of thermal expansion
Q	activation energy of diffusion
k	Boltzmann constant
	atomic volume
D_o	diffusivity coefficient
δ_o	grain boundary width

Microfracture in Brittle Solids

Yen Fu

Master of Science
in Engineering

Materials Science and
Mineral Engineering
Department

Professor Anthony G. Evans
Chairman of Committee

Sponsors: Department of Energy

ABSTRACT

Microcracks can occur in ceramics subject to large localized residual stress, associated with a phase transformation or thermal contraction mismatch. The residual stress field in the absence of cracks can be calculated by using the three-step procedure given by Eshelby. The stress intensity factors for an evolving crack in the stress field can then be calculated by the superposition method. The microcracking process can be evaluated by comparing the stress intensity factors with the local fracture toughness of the material. Two microcracking cases have been studied by this method.

Microcracking associated with the martensitic transformation of ZrO_2 was analyzed. Interfacial dislocations have been proposed as microcrack initiation sites. Calculated stress intensity factors confirm this possibility and provide reasonable values of the interface fracture energy for monoclinic ZrO_2.

The grain boundary residual stresses in single phase polycrystals with thermal contraction anisotropy are calculated for a general configuration of nearby grain orientations. Grain boundary microcracks are possibly initiated from grain triple junction inhomogeneities,

such as cavities. Two equations for predicting the critical grain size for spontaneous microcracking are given which correlate quite well with observations for several materials.

1. Introduction

Certain brittle solids are susceptible to the formation of isolated stable cracks whose sizes are in the range of the microstructural constituents, e.g. grains. These cracks can form either spontaneously[1,2] or due to external loads.[2] In most cases, the microcracks are associated with residual stress fields which arise from shape mismatch between adjacent microstructural constituents. Examples include microcracking in single phase polycrystalline ceramics due to thermal contraction anisotropy[1,2] and microcracking during martensitic phase transformations.[+]

Several physical properties can be influenced by the formation of microcracks. It is observed that microcracking can have a beneficial influence on thermal insulation[4] and, frequently, can enhance the thermal shock resistance. The formation of microcracks can have either beneficial or deleterious effects on mechanical properties, depending on the role of these microcracks. For example, the influence of microfracture on the mechanical strength would be deleterious.[2] In the absence of a discrete macrocrack, materials susceptible to microfracture are subject to damage upon application of an external load. The damage consists of microcracks nucleated at microstructural inhomogeneities. The microcrack density increases with load microcrack coalescence occurs and eventually a discrete macrocrack forms. The macrocrack subsequently propagates to failure. Therefore, the mechanical

---

[+]See Section 3.

strength is dictated by the susceptibility to microfracture. The microcrack nucleation process depends on the magnitude and configuration of the residual stress field. The microcrack coalescence process depends on the distribution of microcrack initiation sites and microcrack interaction. The nature of the former process will be elucidated in the present study.

On the other hand, the formation of microcracks can be beneficial in increasing the fracture toughness.[6] It is observed that a microcrack process zone is sometimes associated with the propagation of the macrocrack. This usually results in an extrinsic toughness in excess of the intrinsic material toughness. The toughening is related to the change in material compliance within the process zone. The problem is, as yet, poorly defined at the quantitative level. Another way of visualizing the toughening process is to consider the creation of microcracks as a source of net energy absorption. However, this also lacks quantitative evidence. The results obtained in the present study will provide some insight into microcrack induced toughening.

Because of the influence of microcracks on the various physical properties, understanding the microcrack formation mechanism has practical implications. Many experimental studies have been conducted to characterize microcracking in single phase polycrystalline ceramics with thermal expansion anisotropy.[1] Therefore, most of the mathematical modeling of the microcracking process has been based on these systems. Initially, an approach based on a maximum stress criterion was proposed.[7] This proved unsuccessful. Subsequently, models

based on an energy balance criterion were developed.[8] These correlate more satisfactorily with experiment. However, the detailed configuration of the residual stress field, which dictates the nucleation of the microcrack, as well as the underlying mechanism of the cracking process, are ignored.

The present study is focused on the microfracture process in martensitic transformations, as well as in single phase polycrystalline material. The residual stress field is calculated, taking into account the microstructure at the microfracture site. A fracture mechanics analysis is then utilized and a detailed understanding of the microcrack evolution process is obtained.

2. General Method of Solution

The general method used for predicting microfracture consists of two parts. The first part, using procedures similar to those given by Eshelby,[9] permits calculation of the residual stress field (due to volume, or shape mismatch) in the absence of cracks. The second part, derived from linear elastic fracture mechanics and using superposition principles, characterizes the evolution of a crack within this stress field.

The residual stress field σ_{ij} (in the absence of cracks) caused by volume contraction mismatch can be calculated in the following way. Imagine the contraction being decomposed into three steps:

1. Let each homogeneous part be separated from its surroundings to permit an unconstrained shape change.

2. Apply surface forces to restore the original shape of each part.

3. Reassemble the components and release the surface forces.

No stresses are created in the first step. In the second step, surface forces $F_i dS$ are applied and stresses σ^T_{ij} are created in each part. σ^T_{ij} can be readily obtained from the free contraction strain ε^T_{ij},

$$\sigma^T_{ij} = - C_{ij} \ \varepsilon^T_k \tag{2.1}$$

ε^T_k (and hence σ^T_{ij}) should be homogeneous in each part. The negative sign appears because each part is being restored to original shape. The magnitude of the surface forces $F_i dS$ can be obtained from the equilibrium conditions at boundaries,

$$F_i dS = \sigma^T_{ij}\, dS_j \tag{2.2}$$

In the third step, additional stresses are created by releasing the surface forces. This is equivalent to the application of body forces $F_i' dS$ opposite in sign to the surface forces $F_i dS$.

$$F_i' dS = - F_i dS \tag{2.3}$$

Stresses created by body forces are more difficult to calculate. Each infinitesimal element of body force, $F_i' dS$, can be treated as a point force. The stresses σ^c_{ij} can thus be obtained by superposition of the infinitesimal stresses $d\sigma^c_{ij}$ created by the point forces $F_i' dS$. Remote from the outer surfaces, the stress field solution for a point force in an infinite body can be used. In two-dimensional situations (see Fig. 1), $d\sigma^c_{ij}$ can be expressed as [10]

$$d\sigma^c_{xx} = \frac{1}{4\pi}\,\frac{\cos\theta}{r}\,[-(3+\nu) + 2(1+\nu)\sin^2\theta]\, F_i' dS$$

$$d\sigma^c_{yy} = \frac{1}{4\pi}\,\frac{\cos\theta}{r}\,[(1-\nu) - 2(1+\nu)\sin^2\theta]\, F_i' dS \tag{2.4}$$

$$d\sigma^c_{xj} = -\frac{1}{4\pi}\,\frac{\sin\theta}{r}\,[(1-\nu) + 2(1+\nu)\cos^2\theta]\, F_i' dS$$

where ν is Poisson's ratio, and r and θ are the radial coordinates as shown in Fig. 1.

The resultant stresses σ_{ij} are obtained by superposition,

$$\sigma_{ij} = \sigma^T_{ij} + \sigma^c_{ij} \tag{2.5}$$

The stress itensity factor K for a crack located within the residual stress field σ_{ij} can be deduced by employing a superposition solution.+ For a symmetrical stress field $\sigma_{yy}(x)$ (see Fig. 2.A),

---

+Here, only Mode I loading is considered equivalent expressions exist for the other two modes.

$$K = 2\sqrt{\frac{c}{\pi}} \int_0^c \frac{\sigma_{yy}(x)}{\sqrt{c^2 - x^2}}\, dx \tag{2.6}$$

for both ends of the crack. For a non-symmetrical stress field $\sigma_{yy}(x)$ (see Fig. 2.B),

$$K = \sqrt{\frac{2}{\pi c}} \int_0^c \frac{\sigma_{yy}(x)\sqrt{x}}{\sqrt{c - x}}\, dx \tag{2.7}$$

for the end of the crack at $x = c$. The calculated stress intensity factor, K, can be compared with the local fracture toughness K_c of the material and the crack evolution (propagation) behavior determined.[12]

3. Microfracture Induced by Phase Transformation in ZrO_2

3.1. Observations

The first analysis of microcrack nucleation is performed for interface microcracking following martensitic transformations in ZrO_2. Martensitic transformation in ZrO_2 invariably requires twin or variants[13] which minimize the macroscopic shape change of the transforming particle. Twin induced microcracks have been observed in a hot pressed Al_2O_3/ZrO_2 material containing a proportion of monoclinic ZrO_2 particles.[14] The observations were conducted using TEM, employing thin foils prepared by a conventional ion milling technique. The detailed characterization of microcracks has been confined to cracks formed at interfaces within the ZrO_2 particles in order to permit an effective comparison with the calculations, which are based upon elastic homogeneity in the vicinity of the microcrack.

Some typical examples of microcracked interfaces are shown in Fig. 3. It is noted that the microcracks occur at alternate interface intersections; evidently, those subject to normal tension at the interface. Also, the crack surface separations are larger than the elastic opening displacements. Some enhancement of the separation during the ion thinning process has thus undoubtedly occurred, particularly within the vicinity of the microcrack centers. The accelerated thinning has improved the detectability of the microcracks, without inducing appreciable changes in the crack length.

The extension of the cracks is restricted in each case to a distance equal to about half of the twin spacing. The crack trajectories

lie approximately along the interface separating the intersecting zones of twins. The appearance of strain contours in the vicinity of the interface indicates that appreciable residual strain is retained, principally in the regions (of compressive normal strain) between the microcracks.

More general observations of twins in ZrO_2 particles, employing tilting procedures, indicate that the twins exhibit a plate-like morphology with an essentially constant plate thickness (for a given transformation mechanism) of 0.03 μm. Another study[15] of the fine structure reveals the existence of dislocations, both along the habit planes and twin interfaces. Such dislocations, as will be shown later, are essential for the nucleation of the interfacial microcracks.

3.2. Stress Analysis

The plate morphology of the twins suggests that the stresses within a thin foil, in the vicinity of the internal interface, can be well approximated by adopting a two-dimensional procedure, based on the method described in Section 2 (Fig. 3). Here, each twin is modeled by a rectangle of constant thickness. After an unconstrained transformation, the twin would become a parallelogram; the major component of strain being a shear γ_T of magnitude = 0.14.[16,17] To restore the shape of each twin, following the steps described in Section 2, surface forces PdS are applied along the boundary of each twin, where PdS is given by

$$PdS = \mu\gamma_T dS \tag{3.1}$$

(μ is the shear modulus, dS is an infinitesimal length of the boundary). The stresses induced in this step are

$$\begin{aligned} \sigma^T_{xx} &= 0 \\ \sigma^T_{xy} &= -\mu\gamma_T \end{aligned} \tag{3.2}$$

In the next step, the surface forces are relaxed by applying body forces P'dS equal but opposite to PdS. The stresses induced by the body forces would have to be calculated from superposition of the stresses induced by each infinitesimal body force P'dS. The alternating shear characteristics of the array indicates that the interface stress should be dominated by the body forces imposed on those boundaries adjacent to the location of interest. The stresses that derive from forces on more remote boundaries are expected to cancel. Therefore, the stresses along the interface induced by a single twin pair are

calculated with other twins and the rest of the surroundings treated as an elastically homogeneous matrix. (Fig. 4) The stresses, induced by body forces, along the twin termination interface are given as (Appendix 1),

$$\frac{\sigma^c_{xx}}{\mu\gamma_T} = \frac{1}{4\pi}\ (3 + \nu)\left\{\ln\left[\left(\frac{d}{a}\right)^2 - 1\right] + \ln\left(\frac{d}{a} + 1\right)\right\}$$

$$\sigma^c_{xy} = -\ \mu\gamma_T \tag{3.3}$$

where a is the distance from the central boundary, and d is the width of one twin. The twin length is assumed to be much larger than d such that the influence of the body forces on the opposite termination interface can be neglected. The final stresses, obtained by combining the transformation stresses expressed in Eq. 3.2 and the constrained stresses expressed in Eq. 3.3, are

$$\sigma_{xx} = \sigma^T_{xx} + \sigma^c_{xx} = \frac{\mu\gamma_T}{4\pi}\ (3 + \nu)\ \left\{\ln\left[\left(\frac{d}{a}\right)^2 - 1\right] + \ln\left(\frac{d}{a} + 1\right)\right\}$$

$$\sigma_{xy} = \sigma^T_{xy} + \sigma^c_{xy} = 0 \tag{3.4}$$

A similar procedure can be used to calculate the stress for any number of twin pairs. The stresses along the central interface for the six twins pertinent to the present observations (Fig. 3) are

$$\frac{\sigma_{xx}}{\mu\gamma_T} = \frac{(3 + \nu)}{4\pi}\left\{\ln\left[\left(\frac{d}{a}\right)^2 - 1\right] + \ln\left[\frac{d}{a} + 1\right] + 2\ \ln\left[\frac{d^2 - a^2}{4\alpha^2 - a^2}\right]\right.$$

$$\left. + 2\ \ln\left[\frac{9d^2 - a^2}{4d^2 - a^2}\right]\right\} \tag{3.5}$$

$$\sigma_{xy} = 0$$

The dimensionless stress $\sigma_{xx}/\mu\gamma_T$ depends exclusively upon the relative distance a/d from the central boundary, as plotted in Fig. 5. The most important characteristics of the stress are the singularities at the interface/boundary intersection. The tensile singularity at the inner boundary is characterized by,

$$\frac{\sigma_{xx}}{\mu\gamma_T} = \frac{3}{4\pi}(3 + \nu)\ \ell n\ \frac{d}{a} \tag{3.6}$$

It will be demonstrated that this singularity dominates the nucleation of microcracks.

A uniform compressive stress that results from the dilational transformation strain is also required for particles fully constrained by the Al_2O_3 matrix. However, this stress is expected to be of negligible magnitude in thin foils, because of a relaxation effect associated with the elastic deflection (buckling) of the foil.

3.3 The Stress Intensity Factor

The logarithmic character of the stress singularity induced by variant formation is probably too weak to permit the formation of a microcrack in the absence of an interface inhomogeneity.[+] Hence, the fracture analysis is conducted by hypothesizing the existence of a crack-like inhomogeneity at the site subject to the maximum stress. The nature of this inhomogeneity will be discussed later. Stress intensity factors can be calculated for the crack-like inhomogeneities and the resultant microcracks, as shown in Section 2. Specifically, for a crack of length 2c symmetrically located in the stress field $\sigma_{xx}(a)$, the stress intensity factor K may be estimated from the superposition solution;

$$K = 2\sqrt{\frac{c}{\pi}} \int_0^c \frac{\sigma_{xx}(a)}{\sqrt{c^2 - a^2}}\, da \tag{3.7}$$

Inserting the stress field σ_{xx} of six variants obtained from Eq. 3.5 and integrating, yields the numerical result for K plotted in Fig. 6. The occurrence of the maximum in K is typical of crack behavior in rapidly varying stress fields (consistent with observations of crack arrest).

[+]A singularity with a strength $\geq 1/x$ (the crack tip singularity) can be readily demonstrated to induce fracture in the absence of inhomogeneities. However, fracture in the presence of weaker singularities is not well understood. It is presumed here that weaker singularities are incapable of crack nucleation.

Numerical integration is needed because terms like $\int_0^c \frac{1}{\sqrt{c^2-a^2}} \ln \frac{1}{a} da$ cannot be integrated in closed form.

The evolution of microcracks can be examined by comparing this K curve with the crack propagation resistance of the material. This comparison will be conducted in the following section.

3.4. Analysis of Microfracture

The two most pertinent features of the microcrack observations upon which the subsequent argument is based are (a) the incidence of microcracking at each junction, and (b) the (absolute) magnitude of the crack arrest length. Firstly, consider the observed invariance of microcrack formation at interface junctions. These junctions were originally located within a single grain (particle) of tetragonal ZrO_2. Postulates for fracture based on the prior existence of inhomogeneities of appreciable size are thus necessarily obviated (because there can be no rationale for anticipating inhomogeneities of relatively large size at each junction). The largest crack-like inhomogeneities that can consistently occur along the termination interface of a variant are interfacial dislocations, as observed in a comparison study.[15] The following analysis, which attempts to trace the evolution of the microcracks, invokes interfacial dislocations of edge character. A similar analysis could be performed for mixed dislocations.

An edge dislocation core contains a small zone (on the tensile side) with crack-like characteristics, as first noted by Stroh[18] (Fig. 7). Additionally, the dislocation self-stress will locally augment the stress intensity factor. It can be readily demonstrated that the stress field associated with an edge dislocation provides a stress intensification analogous to that of a crack subject to a semi-infinite wedge opening, as provided by the extra half plane[11] (Fig. 7), where

$$K = \frac{\sqrt{2}\,\mu b\,(1 + \nu)}{\pi\sqrt{c}} \tag{3.8}$$

b is the thickness of the wedge (approximately equal to the Burgers vector) and c is the length of the crack ahead of the wedge. The magnitude of the stress intensity factor increases with decrease in crack length (Fig. 7) and is, of course, only approximate at very small crack lengths (when non-linear effects become important).

The stress intensity factors from the dislocation field and the variant field can be superimposed to provide the final trend in K with crack length, as shown schematically in Fig. 8. A minimum, K_{min}, now appears in addition to the previously noted maximum. The level of this minimum has a major influence upon the onset condition for microcracking. Specifically, when K_{min} exceeds the crack extension resistance of the interface K_{IC}^{inter}, a well developed microcrack will form with an approximate final length, C_f, as illustrated in Fig. 9.

Variations in K_{min} that elevate it to the requisite level for microcrack formation are dictated by the amplitude and the scale of the stress field induced by the variants. However, inspection of Fig. 9 indicates that conformance of the K level with these microcrack formation requirements can be directly deduced from the final crack length. This is achieved by superimposing the crack length measured from Fig. 3 onto the K curve calculated for the observed variant structure. The K level at the intersection (as well as providing a measure of the nominal crack propagation resistance of the interface) must be less than K_{min} to account for microcrack initiation at edge dislocations.

The specific results of this procedure are presented in Fig. 10. The absolute magnitude of K was deduced by employing the measured value of d(300 Å), the known values for μ(69GPa) and ν(0.25) and estimates for γ_T and b. The variant shear strain γ_T is taken to be $\geq$ 0.14, (a minimum value for transformations in ZrO_2) and b is assumed to be ~ 5 Å, the unit cell dimension in the monoclinic structure. Superimposing the measured C_f/d of 0.5 yields the intersection shown in Fig. 10. The intersection K level (1.8 MPa $\sqrt{m}$) is just below K_{min} (2.15 MPa$\sqrt{m}$) as required to account for the formation of a microcrack at an interface edge dislocation. The nominal interface crack propagation resistance given by the interaction level is K_{IC}^{inter} = 1.8 MPa m (g_c^{inter} = 18 Jm^{-2}). This value is at the lower bound of the range typically measured for polycrystals of cubic ZrO_2, g_c = 16 - 40 Jm^{-2}.[19,20] and can thus be regarded as consistent with reasonable expectations for interface separation in ZrO_2.

3.5 Discussion

A relatively consistent description of microcrack nucleation based upon the combined stress fields of an edge dislocation and of martensite variants has been provided. This is the first example of microcrack formation in ceramics that has not required either the pre-existence of a microstructural inhomogeneity (such as a void or an inclusion) or a dislocation slip band. The microcracking process is similar to that proposed by Stroh, for crack nucleation ahead of a dislocation pile-up, but excludes the necessity for dislocation coalescence (which is a central feature of the Stroh mechanism). Since dislocation mobility is rather limited in ceramics, the capability for crack nucleation without invoking dislocation motion is probably of more general interest.

The extension of the present nucleation concept to other microcrack situations is evidently a subject for further detailed examination. However, it is observed here that the variables which dictate microcrack formation are appreciably different for other common microcrack problems. The most notable is microcracking at grain boundaries from thermal contraction anisotropy, which will be analysed in the next section.

4. Microcracking in Single Phase Polycrystals

4.1. Observations

In the previous section, microcracking during martensitic transformations in ZrO_2 was analysed. Microcracking also occurs at grain boundaries in single phase polycrystalline ceramics with thermal expansion anisotropy.[1,2] In such cases, microcracks are created by residual stresses induced when the material is cooled from a high temperature. The residual stresses begin to develop when relaxation through diffusion becomes inoperative below a temperature Tg.[21]

One of the dominant features of such microcracking events is the dependence on grain size. Typically, there is a critical grain size, ℓ_c, below which microcracking is greatly suppressed and above which a significant density of microcracks becomes evident. The ability to predict ℓ_c is a primary objective of microcracking analysis.

Previous attempts at describing microcracking have included a tensile stress criterion (which does not yield a grain size dependence, because the amplitude of the residual stress field is independent of the grain size), and an energy balance criterion. The latter equates the loss in strain energy associated with complete separation of a boundary facet to the increase in surface energy, and yields a critical facet length,[1]

$$\ell_c = \frac{24\ \gamma_{g.b.}}{E\ \varepsilon^2} \tag{4.1}$$

where E is Young's modulus, $\gamma_{g.b}$ is the grain boundary fracture energy and ε is the grain boundary strain. However, only the initial and

final stages of the formation event are considered in the thermodynamic analysis; whereas, fracture is dictated by the rate of energy change at the critical condition for unstable crack extension.

In the present analysis, the grain size effect is shown to stem directly from considerations related to the gradient of the residual stress field (stress intensity factor criterion) and/or to the stress relaxation effects.[21]

4.2. Stress Analysis

First, the residual stress field induced by thermal contraction mismatch is calculated along one grain boundary facet. Assuming a uniform grain size, a two dimensional array of hexagons (Fig. 11) can be used to model the system. Each grain has a random orientation, and elastic anisotropy is neglected (to permit the use of stress functions derived from isotropic elasticity). This simplification should not introduce important quantitative errors because the thermal stresses are relatively insensitive to the elastic anisotropy (in contrast to their strong dependence on the thermal expansion anisotropy).[22]

To carry out the calculation, the system is further simplified by concentrating only on the four grains nearest to the grain boundary, while treating the remainder of the system as an elastically homogeneous matrix. (Fig. 11) Following the first step in section 2, the four grains are separated from the matrix and allowed to contract freely. The strain $^{T}_{c}$ of the "matrix cavity" is then uniform and isotropic and given by;

$$\varepsilon_c^T = -\langle\alpha\rangle \ \Delta T \tag{4.2}$$

where α is the isotropic expansion coefficient of the matrix and ΔT is for temperature range over which the stresses develop. The strains in the principal directions of each grain are

$$\begin{aligned} \varepsilon &= -\alpha_{\ell} \ \Delta T \\ \varepsilon_s &= -\alpha_s \ \Delta T \end{aligned} \tag{4.3}$$

where $\alpha_{\ell,s}$ are the linear expansion coefficients of the grain. The magnitude of $\langle\alpha\rangle$ is between the magnitudes of α_ℓ and α_s.

Next, surface forces are applied on the boundaries of each grain in order to restore the regular hexagonal grain shape, before replacing the grains into the matrix cavity. The strains created in each grain are readily obtained as

$$\begin{aligned} \varepsilon^T_\ell &= (\alpha_\ell - \langle\alpha\rangle)\Delta T \equiv \Delta\alpha_\ell \Delta T \\ \varepsilon^T_s &= (\alpha_s - \alpha)\Delta T = -(\langle\alpha\rangle - \alpha_s)\ \Delta T \equiv -\Delta\alpha_s \Delta T. \end{aligned} \tag{4.4}$$

The stresses within the grain would be

$$\begin{aligned} \sigma^T &= \langle E\rangle (\Delta\alpha_\ell - \nu\Delta\alpha_s)\Delta T/(1-\nu^2) \\ \sigma^T_s &= \langle E\rangle (\Delta\alpha_s - \nu\Delta\alpha)\Delta T/(1-\nu^2) \end{aligned} \tag{4.5}$$

where $\langle E\rangle$ is the isotropic Young's modulus and ν is the Poisson's ratio. The surface forces needed to deform each grain can be obtained from the equilibrium conditions on the boundaries. They are shown in Fig. 12 for each boundary section of a hexagonal grain.

In the next step, these surface forces are released by applying body forces equal in magnitude but opposite in sign to the surface forces. These body forces would induce additional stresses σ^c_{ij} within each grain and the matrix. To calculate these stresses, the body force on an infinitesimal boundary segment is treated as a line force in a plate, Eq. 2.4. The stresses induced by body forces on each segment are added to give the resultant σ^c_{ij}. It is convenient to establish the stress field of distributed forces on a line seg-

ment before proceeding. The stress field, as shown in Appendix 2, is given by

$$\sigma^c_{yy} = \frac{P_x}{4\pi}[(1-\nu)F_2 + 2(1+\nu)F_3] + \frac{P_y}{4\pi}[(3+\nu)F_1 - 2(1+\nu)F_4]$$
$$\sigma^c_{xy} = \frac{P_x}{4\pi}[(1-\nu)F_1 + 2(1+\nu)F_4] + \frac{P_y}{4\pi}[(1-\nu)F_2 + 2(1+\nu)F_3] \tag{4.6}$$

where F_i's are functions of R, , β, δ which are specified in Appendix 2. By inserting appropriate sets of R, , β, δ values, the stresses created by body force on all boundary segments (except the central segment), can be obtained. The F_i's are rather complex functions (event though in closed forms) and a computer code is used to obtain numerical solutions. The stresses created by body forces on the central boundary segment would be (see Appendix 1)

$$\sigma^c_{yy} = -\frac{1}{2}P_y$$
$$\sigma^c_{xy} = -\frac{1}{2}P_x \tag{4.7}$$

at points close to and above the segment. The constrained stresses σ^c_{ij} are obtained from superposition of stresses created by body forces on the 19 boundary segments. The resultant stresses would be the sum of the transformation stresses σ^T_{ij} and the constrained stresses σ^c_{ij}.

The stresses along one grain boundary calculated with this method for several different configurations of near-by grain orientations are shown in Fig. 13. The tensile stresses approach infinity at grain

triple points. This singularity is dictated by the logarithmic terms in Eq. 4.5, which are explicit in Appendix 2.

To analyse the problem of critical grain size, we concentrate on the grain boundary subject to the largest tensile stress. It is observed in Fig. 13 that the tensile stress is largest for configuration A, in which the two grains adjacent to the grain boundary have their maximum contractions in a direction perpendicular to the boundary. The amplitude of this stress field is independent of the grain size. Also, the singularity at the triple point prohibits the derivation of a critical grain size from the stress field. Therefore, we proceed to calculate the stress intensity factor of a crack of size c enplaced within the stress field.

4.3 The Critical Microcracking Condition

As described in section 2, the stress intensity factor of a crack can be obtained from the original crack-free stress field by using Eq. 2.7. Inserting into Eq. 2.7 the stress field of the grain boundary under maximum tension in Fig. 13.A, the stress intensity factors of an evolving grain boundary crack with one end fixed at the grain triple point can be obtained. Here a numerical method is needed to calculate the integral in Eq. 2.7. The result is shown in Fig. 14, where the normalized stress intensity factor versus normalized crack size is plotted. The qualitative dependence of microcracking on the grain size can be derived from this figure. Notice that the stress intensity factor is normalized by the square root of grain size. Hence, by changing the ordinate into an absolute scale and plotting the stress intensity factors for constant grain size, higher levels of the stress intensity factor would obtain for larger grained materials. This implies that microcracking would be more severe for larger grained structures.

The general characteristics of the stress intensity curve indicate several important features. Firstly, the stress intensity approaches zero as the crack size becomes small. Hence, inhomogeneities located at triple junctions are needed to initiate microcracking. This is a similar requirement to that established for microcracking in ZrO_2, where microcracks were predicted to initiate from interfacial dislocations. However, the inhomogeneities required at the triple junctions must be much more extensive in dimension than dislocations. The most

viable possibilities include cavities, inclusions, etc.; although, the explicit role of the inhomogeneities on crack initiation is not well understood. As an approximation, these inhomogeneities are treated as crack-like entities, such that the level and variation of the stress intensity factor can be directly related to the size and shape of the inhomogeneity. This approximation is subsequently used for establishing crack initiation criteria.

Secondly, the stress intensity factor exhibits a maximum. This maximum can be associated with a lower bound on the microcrack initiation condition; a bound which necessitates the pre-existence of an inhomogeneity with relative dimensions $c/\ell \approx 0.2$. Analogous lower bound treatments have been particularly useful in other fracture threshold problems, such as indentation fracture. Finally, it is noted that the stress intensity factor diminishes slowly with crack length beyond the maximum. This contrasts with the rapid decline in the ZrO_2 microcracking problem. Hence, a microcrack, once initiated, is likely to extend across the entire grain facet. The arrest of the microcrack beyond the three grain junction will be dictated by the level of compression on the neighboring grain boundaries.

The grain size dependence of microcracking can be quantified by adopting pertinent initiation criteria. Two such criteria will be adopted herein. Firstly, a lower bound is determined by equating the peak value of K to Kc. From Fig. 12,

$$\frac{5(1-\nu^2)\ K_{max}}{4E\Delta\alpha\Delta T\ \sqrt{\ell_c}} = 1.1 \tag{4.8}$$

Also, Kc is related to the grain boundary fracture energy by

$$2\gamma_{g.b} = \mathcal{G}_c = \frac{K_c^2\ (1-\nu^2)}{E} \tag{4.9}$$

The critical grain size thus becomes

$$\ell_c = \frac{3.1\ \gamma_{g.b.}\ (1-\nu^2)}{E(\Delta\alpha\Delta T)^2} \tag{4.10}$$

An alternate criterion assumes that the effective size of the inhomogeneity is about one tenth of the grain size, typical of the size of residual cavities observed in sintered products. The crack initiation condition would then be $K = K_c$ at $c/\ell = 0.1$. The predicted critical grain size then becomes

$$\ell_c = \frac{3.7\ \gamma_{g.b.}\ (1-\nu)^2}{E\ (\Delta\alpha\Delta T)^2}\ . \tag{4.11}$$

Inserting appropriate values of $\gamma_{g.b.}$, E, ν, ΔT and $\Delta\alpha$ into the equations, the critical sizes can be calculated and compared with the observed values, summarized in Table 1.

A final determination of the critical size requires that ΔT be specified, by virture of a selection of the 'freezing temperature' T_g at which stress relaxation by diffusion terminates. A grain boundary diffusion model[23] indicates that this freezing temperature is given by

$$T_g \sim \frac{Q/k}{n[12\Omega D_o \delta_o E/\sqrt{3}\ n\ k\ \ell^3 \dot{T}]} \tag{4.12}$$

where Q is the activation energy of grain boundary diffusion, k is the Boltzman constant, Ω is the effective volume of the diffussing particles, δ_b is the effective thickness of the grain boundary, E is the Young's modulus, ℓ is the grain size, n is a material dependent parameter and $\dot{T}$ is the cooling rate.

Extension of the analysis to include determinations of the crack density, crack tip process zone etc. requires that relations be established between the stress intensity factor and crack size for general grain orientation configurations. In the present work, the stress intensity factor-crack size relation has only been determined for one configuration (Fig. 13.A), where the tension is a maximum, although the stress analysis has been carried out for a general configuration. The mathematics associated with the general problem are unwieldy, but further analysis seems promising. Subsequent studies will seek reasonable simplifications for the stress fields, and then proceed to predict crack densities.

5. Conclusion

Microfracture is an important phenomenon in brittle materials. Its role can be either deleterious or beneficial. To achieve optimal control, understanding of the initiation and growth mechanisms is essential.

The present study is focused on microfracture both as a consequence of the martensitic transformation in ZrO_2 and in single phase polycrystalline ceramics with thermal contraction anisotropy. In both cases, the microcracks are induced by the residual stress field which arises from shape mismatch (due to either phase transformation or thermal contraction anisotropy). The residual stress field in the absence of the microcracks can be calculated using Eshelby's method. The stresses induced by the body forces are derived from the stress field of a concentrated force in an infinite plate. All the residual stress fields show a logarithmic singularity at the crack initiation site.

The stress intensity factor of an evolving crack in this residual stress field can be calculated using fracture mechanics methods. The initiation and growth processes of the crack can then be derived from comparison of the stress intensity factor with the fracture toughness.

In both cases, it is observed that inhomogeneities are required to initiate the cracks. For microfracture, caused by martensitic transformation in ZrO_2, it has been demonstrated that the interfacial microcracks can be initiated from edge dislocations. However, for microfracture in single phase polycrystalline ceramics, the initiation mechanism is not fully understood. The inhomogeneities could be cavi-

ties or inclusions at grain triple points. Two approximate initiation criteria are shown which can be used to derive the critical grain size for spontaneous microfracture. Other qualitative aspects of grain size dependence for microfracture in single phase polycrystalline ceramics can also be derived. Another factor which can influence the grain size dependence is the grain size dependence of the diffusion relaxation of the residual stress field that occurs above the freezing temperature. It is shown that such a factor can be incorporated in the present analysis.

ACKNOWLEDGMENTS

The author wishes to thank Professor Anthony G. Evans for his continuous guidance and encouragement in this research work. Further thanks are extended to Professor Lutgard C. DeJonghe and Andreas M. Glaeser for their helpful advices. This work was supported by the Director, Office of Energy Research, Office of Basic Energy Sciences, Materials Science Division of the U. S. Department of Energy under Contract No. W-7405-ENG-48.

Appendix 1: Stresses Induced By Body Forces For One Twin Pair

For one twin pair, there are seven straight boundary sections which are labeled from (1) to (7) as shown in Fig. 4. The body forces are of magnitude $\mu\gamma_T$ per unit length on the outer boundaries and of magnitude $2\mu\gamma_T$ per unit length on the inner boundary section (3). The directions of these forces are as shown by the arrows in Fig. 14. The stresses induced by the body forces on each boundary section are calculated separately and then summed. Each boundary section is cut into infinitesimal segments such that the body forces on each segment dS can be treated as a concentrated force $\mu\gamma_T dS$ ($2\mu\gamma_T$ dS on boundary section (3)) in an infinite plate (Fig. 1) where the stress field is

$$d\sigma_{xx} = \frac{\mu\gamma_T dS}{4\pi} \frac{\cos\theta}{r} [-(3+\nu) + 2(1+\nu)\sin^2\theta]$$

$$d\sigma_{yy} = \frac{\mu\gamma_T dS}{4\pi} \frac{\cos\theta}{r} [(1-\nu) - 2(1+\nu)\sin^2\theta] \qquad \text{(A1.1)}$$

$$d\sigma_{xy} = -\frac{\mu\gamma_T dS}{4\pi} \frac{\sin\theta}{r} [(1-\nu) + 2(1+\nu)\cos^2\theta]$$

I. Stresses induced by body forces on boundary section (1)

Calculation of these stresses represent a special case, because the stress location coincides with the boundary section (1) (see Fig. 4) and the stress across the boundary is discontinuous (positive on one side and negative on the other). Therefore, positions infinitesimally close to the boundary are selected for the computation.

Close to the boundary, the boundary section (1) can be regarded as infinitely long (Fig. 15).

Consider a position P at a distance h from the boundary and an angle α to the boundary segment dS. The stress induced at P by body forces $\mu\gamma_T dS$ on dS would then be (from Eq. A1.1)

$$d\sigma_{xx} = \frac{\mu\gamma_T dS}{4\pi} \quad \frac{\cos(\frac{\pi}{2} + \alpha)}{h/\cos\alpha} \left[(1-\nu) - 2(1+\nu)\sin^2(\frac{\pi}{2} + \alpha)\right]$$

$$d\sigma_{xy} = -\frac{\mu\gamma_T dS}{4\pi} \quad \frac{\sin(\frac{\pi}{2} + \alpha)}{h/\cos\alpha} \left[(1-\nu) + 2(1+\nu)\cos^2(\frac{\pi}{2} + \alpha)\right] \tag{A1.2}$$

Replacing $dS = h\, d\alpha/\cos^2\alpha$ and integrating from $\alpha = -\pi/2$ to $\alpha = +\pi/2$, Eq. A1.2 becomes

$$\sigma_{xx} = 0^{+}$$

$$\sigma_{xy} = -\frac{1}{2}\mu\gamma_T \tag{A1.3}$$

This is the stress field at a point infinitesimally close to the boundary. Across the boundary, the stress field would change abruptly to

$$\sigma_{xx} = 0$$

$$\sigma_{xy} = \frac{1}{2}\mu\gamma_T \tag{A1.4}$$

+If the normal body force component F_x is not zero (see Fig. 15) σ_{xx} would be $-\frac{1}{2}F_x$.

II. Stresses induced by body forces on boundary sections (2) - (4)

Comparing with Fig. 1, the parameters r and θ for segments on boundary sections (2) - (4) can be obtained as shown in Fig. 4. r and θ in each case can be expressed by a, d and S.

For section (2),

$$r^2 = (d-a)^2 + S^2 \tag{A1.5}$$

$$\cos\theta = \frac{S}{[(d-a)^2 + S^2]^{1/2}} \qquad \sin\theta = \frac{d-a}{[(d-a)^2 + S^2]^{1/2}}$$

For section (3),

$$r^2 = a^2 + S^2$$

$$\cos\theta = -\frac{S}{(a^2 + S^2)^{1/2}} \qquad \sin\theta = \frac{a}{(a^2 + S^2)^{1/2}} \tag{A1.6}$$

For section (4),

$$r^2 = (a + d)^2 + S^2$$

$$\cos\theta = \frac{d + a}{\left[(d + a)^2 + S^2)\right]^{1/2}} \qquad \sin\theta = -\frac{S}{\left[(d + a)^2 + S^2)\right]^{1/2}} \tag{A1.7}$$

Substituting these into Eq. A1.1 and integrating from $S = 0$ to $S = \ell$, we obtain

for section (2)

$$\sigma_{xx} = -\frac{\mu\gamma_T}{8\pi}(3+\nu)\,\ell n\left[1+\left(\frac{\ell}{d-a}\right)^2\right] - \frac{\mu\gamma_T}{4\pi}(1+\nu)\left[\frac{(d-a)^2}{(d-a)^2+\ell^2}-1\right]$$

(A1.8)

$$\sigma_{xy} = -\frac{\mu\gamma_T}{4\pi}\left[2\tan^{-1}\frac{\ell}{(d-a)} - (1+\nu)(d-a)\frac{\ell}{\ell^2+(d-a)^2}\right]$$

for section (3),

$$\sigma_{xx} = \frac{\mu\gamma_T}{4\pi}(3+\nu)\,\ell n\left[1+\left(\frac{\ell}{a}\right)^2\right] + \frac{\mu\gamma_T}{2\pi}(1+\nu)\left[\frac{a^2}{\ell^2+a^2}-1\right]$$

(A1.9)

$$\sigma_{xy} = -\frac{\mu\gamma_T}{2\pi}\left[2\tan^{-1}\frac{\ell}{a} - (1+\nu)\frac{\ell a}{{}^2+a^2}\right]$$

for section (4),

$$\sigma_{xx} = -\frac{\mu\gamma_T}{8\pi}(3+\nu)\,\ell n\left[1+\left(\frac{\ell}{d+a}\right)^2\right] - \frac{\mu\gamma_T}{4\pi}(1+\nu)\left[\frac{(d+a)^2}{\ell^2+(d+a)^2}-1\right]$$

(A1.10)

$$\sigma_{xy} = \frac{\mu\gamma_T}{4\pi}\left[2\tan^{-1}\frac{\ell}{d+a} - (1+\nu)(d+a)\frac{\ell}{\ell^2+(d+a)^2}\right]$$

Since $\ell >> d$, these equations can be simplified by letting $\ell \to \infty$. Summing the simplified equations gives:

$$\sigma_{xx} = \frac{\mu\gamma_T}{4\pi}(3+\nu)\,\ell n\left[\left(\frac{d}{a}\right)^2 - 1\right]$$

(A1.11)

$$\sigma_{xy} = -\frac{1}{2}\mu\gamma_T$$

III. Stresses induced by body forces on boundary section (5)

Substituting $r = s + a$, $\theta = \pi$ into Eq. A1.1 and integrating from $S = 0$ to $S = d$, we obtain

$$\sigma_{xx} = \frac{\mu\gamma_T}{4\pi}(3+\nu)\,\ell n\left(\frac{d}{a} + 1\right)$$

$$\sigma_{xy} = 0 \qquad \text{(A1.12)}$$

IV. Stresses induced by body forces on boundary sections (6) - (7)

For boundary sections (6) - (7), $r \approx \ell >> d$. The terms in Eq. 1 $\frac{\sin\theta}{r}$ and $\frac{\cos\theta}{r}$, would approach zero. Therefore, the stresses induced by body forces on boundary sections (6) - (7) should be negligible.

V. Resultant stresses

Summing Eqs. A1.3, A1.11 and A1.12, we obtain the resultant stresses at the termination interface induced by body forces on the boundary of a twin pair

$$\sigma^c_{xx} = \frac{\mu\gamma_T}{4\pi}(3+\nu)\left\{\ell n\left[\left(\frac{d}{a}\right)^2 - 1\right] + \ell n\left[\frac{d}{a} + 1\right]\right\}$$

$$\sigma^c_{xy} = -\,\mu\gamma_T \qquad \text{(A1.13)}$$

Appendix 2: Stress Field of Distributed Force in Infinite Plate

Distributed forces P_x and P_y per unit length act on the line segment of length ℓ. Consider the stresses at a point where R and δ are the distance and angle from one end of the line segment (Fig. 16). Forces on an infinitesimal segment $d\ell$ can be treated as a concentrated line force. Comparing with Fig. 1, we obtain

$$d\sigma_{yy} = \frac{P_x dS}{4\pi} \frac{\cos(\pi+\phi)}{r} [(1-\nu)-2(1+\nu)\sin^2(\pi+\phi)]$$

$$+ \frac{P_y dS}{4\pi} \frac{\cos\left(\frac{\pi}{2}+\phi\right)}{r}\left[- (3-\nu)-2(1+\nu)\sin^2\left(\frac{\pi}{2}+\phi\right)\right]$$

$$d\sigma_{xy} = - \frac{P_x dS}{4\pi} \frac{\sin(\pi+\phi)}{r} [(1-\nu) + 2(1-\nu)\cos^2(\pi+\phi)] \qquad \text{(A2.1)}$$

$$- \frac{P_y dS}{4\pi} \frac{\sin\left(\frac{\pi}{2}+\phi\right)}{r}\left[- (1-\nu)+2(1+\nu)\cos^2\left(\frac{\pi}{2}+\phi\right)\right]$$

By superposition,

$$\sigma_{yy} = \int_0^{\ell} d\sigma_{yy} \qquad \sigma_{xy} = \int_0^{\ell} d\sigma x_y \qquad \text{(A2.2)}$$

There are four characteristic integration terms,

$$\int_0^{\ell} \frac{\sin\phi}{r}\, dS \equiv F_1$$

$$\int_0^{\ell} \frac{\cos\phi}{r}\, dS \equiv F_2$$

$$\int_0^{\ell} \frac{\cos\phi \sin^2\phi}{r}\, dS \equiv F_3 \qquad \text{(A2.3)}$$

$$\int_0^{\ell} \frac{\sin\phi \cos^2\phi}{r}\, dS \equiv F_4$$

Expressing r, $\sin\phi$, $\cos\phi$ in R, δ. S, β, gives

$$r^2 = (R \sin\delta + S \sin\beta)^2 + (R \cos\delta + S \cos\beta)^2$$

$$\sin\phi = \frac{R \sin\delta + S \sin\beta}{r}$$

$$\cos\phi = \frac{R \cos\delta + S \cos\beta}{r} \qquad \text{(A2.4)}$$

Substituting these into the four characteristic integrations

$$F_1 = \int_0^{\ell} \frac{\sin\phi}{r}\, dS = \int_0^{\ell} \frac{R \sin\delta + S \sin\beta}{(R \sin\delta + S \sin\beta)^2 + (R \cos\delta + S \cos\beta)^2}\, dS$$

$$= -\frac{\sin\beta}{2} G_1 + \frac{\sin\delta - \sin\beta \cos(\beta-\delta)}{|\sin(\beta-\delta)|} G_2 \qquad \text{(A2.5)}$$

$$F_2 = \int_0^{\ell} \frac{\cos\phi}{r}\, dS$$

$$= -\frac{\cos\beta}{2} G_1 + \frac{\cos\delta - \cos\beta \cos(\beta-\delta)}{|\sin(\beta-\delta)|} G_2$$

$$F_3 = \int_0^{\ell} \frac{\cos\phi \sin^2\phi}{r} dS$$

$$= R \sin^2\delta \cos\delta \left\{ \frac{\ell - R\cos(\beta-\delta)}{2\sin^2(\beta-\delta)\, G_3} + \frac{\cos(\beta-\delta)}{2R\sin^2(\beta-\delta)} + \frac{1}{2R|\sin(\beta-\delta)|} G_2 \right\}$$

$$+ (\sin^2\delta \cos\beta + \sin 2\delta \sin\beta) \left\{ \frac{R^2 - 2R\ell\cos(\beta-\delta)}{2\sin^2(\beta-\delta)\, G_3} - \frac{1}{2\sin^2(\beta-\delta)} - \frac{\cos(\beta-\delta)}{2|\sin^3(\beta-\delta)|} G_2 \right\}$$

$$+ (\sin\delta \sin 2\beta + \cos\delta \sin^2\beta) \left\{ \frac{R\ell[2\cos^2(\beta-\delta)-1] - R^2\cos(\beta-\delta)}{2\sin^2(\beta-\delta)\, G_3} + \frac{\cos(\beta-\delta)}{2\sin^2(\beta-\delta)} + \frac{1}{2|\sin^3(\beta-\delta)|} G_2 \right\}$$

$$- \frac{\sin^2\beta \cos\beta}{2} G_1$$

$$- \frac{\sin^2\beta \cos\beta \cos(\beta-\delta)}{|\sin(\beta-\delta)|} G_2$$

$$- \sin^2\beta \cos\beta \cos(\beta-\delta) \left\{ \frac{[4R^2\cos^2(\beta-\delta) - 2R^2]\ell - 2R^3\cos(\beta-\delta)}{2R\sin^2(\beta-\delta)\, G_3} + \frac{\cos(\beta-\delta)}{\sin^2(\beta-\delta)} + \frac{1}{|\sin^3(\beta-\delta)|} G_2 \right\}$$

$$+ \sin^2\beta \cos\beta \left\{ \frac{+R\ell\cos(\beta-\delta) - R^2}{2\sin^2(\beta-\delta)\, G_3} + \frac{1}{2\sin^2(\beta-\delta)} + \frac{\cos(\beta-\delta)}{2\sin^3(\beta-\delta)} G_2 \right\}$$

$$F_4 = \int_0^{\ell} \frac{\sin\phi \cos^2\phi}{r} dS$$

$$= -\frac{\cos^2\beta \sin\beta}{2} G_1$$

$$- \frac{\cos^2\beta \sin\beta \cos(\beta-\delta)}{|\sin(\beta-\delta)|} G_2$$

$$+ \cos^2\delta \sin\delta \left\{ \frac{R\ell - R^2\cos(\beta-\delta)}{2 \sin^2(\beta-\delta)\, G_3} + \frac{\cos(\beta-\delta)}{2 \sin^2(\beta-\delta)} + \frac{1}{2 \sin(\beta-\delta)} G_2 \right\}$$

$$+ (\cos^2\delta \sin\beta + \sin 2\delta \cos\beta) \left\{ \frac{R^2 - 2R\ell\cos(\beta-\delta)}{2 \sin^2(\beta-\delta)\, G_3} - \frac{1}{2 \sin^2(\beta-\delta)} - \frac{\cos(\beta-\delta)}{2|\sin^3(\beta-\delta)|} G_2 \right\}$$

$$+ (\cos\delta \sin 2\beta + \sin\delta \cos^2\beta) \left\{ \frac{R\ell[2\cos^2(\beta-\delta)-1] - R^2\cos^2(\beta-\delta)}{2 \sin^2(\beta-\delta)\, G_3} + \frac{\cos(\beta-\delta)}{2\sin^2(\beta-\delta)} + \frac{1}{2|\sin^3(\beta-\delta)|} G_2 \right\}$$

$$+ \cos^2\beta \sin\beta \left\{ \frac{R\ell\cos(\beta-\delta) - R^2}{2 \sin^2(\beta-\delta)\, G_3} + \frac{1}{2 \sin^2(\beta-\delta)} + \frac{\cos(\beta-\delta)}{2|\sin^3(\beta-\delta)|} G_2 \right\}$$

$$- \cos^2\beta \sin\beta \cos(\beta-\delta) \left\{ \frac{[4R\cos^2(\beta-\delta) - 2R]\,\ell - 2R^2\cos(\beta-\delta)}{2 \sin^2(\beta-\delta)\, G_3} + \frac{\cos(\beta-\delta)}{\sin^2(\beta-\delta)} + \frac{1}{|\sin^3(\beta-\delta)|} G_2 \right\}$$

where

$$G_1 = \ln \left\{ \frac{\ell^2 - 2R\ell\cos(\beta-\delta) + R^2}{R^2} \right\}$$

$$G_2 = \tan^{-1} \frac{\ell - R\cos(\beta-\delta)}{R|\sin(\beta-\delta)|} - \tan^{-1} \frac{\cos(\beta-\delta)}{|\sin(\beta-\delta)|}$$

$$G_3 = R^2 - 2R\ell\cos(\beta-\delta) + \ell^2$$

Substituting into Eq. A2.1, we obtain

$$\sigma_{yy} = \frac{P_x}{4\pi} [(1-\nu) F_2 + 2(1+\nu) F_3] + \frac{P_y}{4\pi} [(3+\nu) F_1 - 2(1+\nu) F_4] \tag{A2.6}$$

$$\sigma_{xy} = \frac{P_x}{4\pi} [+(1-\nu) F_1 + 2(1+\nu) F_4] + \frac{P_y}{4\pi} [-(1+\nu) F_2 + 2(1+\nu) F_3]$$

References

1. A. G. Evans, Acta Met. 26, 1845 (1978).
2. J. A. Kuszyk and R. C. Bradt, J. Am. Ceram. Soc. 56, 420 (1973).
3. F. A. McClintock and H. J. Mayson, ASME Applied Mechanics Conf. (June 1976).
4. H. J. Siebenbeck, D. P. H. Hasselman, J. J. Cleveland and R. C. Bradt, K. Am. Ceram. Soc. 59, 241 (1976).
5. D. P. H. Hasselman, J. Am. Ceram. Soc. 52, 600 (1969).
6. R. G. Hoagland, G. T. Hahn and A. R. Rosenfield, Rock Mechanics, 5, 77 (1973).
7. W. D. Kingery, H. K. Bowen and D. R. Uhlmann, "Introduction to Ceramics," 2nd ed., John Wiley a Sons, New York (1976).
8. R. W. Davidge and G. Tappin, J. Meter. Sci. 3, 297 (1968).
9. J. D. Eshelby, Proc. Roy. Soc. A241, 376 (1957).
10. S. Timoshenko and J. N. Goodier, "Theory of Elasticity," McGraw-Hill, New York (1950).
11. G. C. Sih, "Handbook of Stress Intensity Factors," Lehigh University Press (1973).
12. B. R. Lawn and T. R. Wilshaw, "Fracture of Brittle Solids," Cambridge University Press, Cambridge (1975).
13. A. G. Evans, N. H. Burlingame, M. Drory and W. M. Kriven, Acta Met. 29, 447 (1981).
14. N. H. Burlingame, M. S. Thesis, University of California, Berkeley (1980).
15. M. Kirn and M. Ruhle, to be published.

16. W. M. Kriven, M. D. Huang and A. G. Evans, to be published.

17. G. Bansal and A. H. Heuer, Acta Met. 22, 490 (1974).

18. A. N. Stroh, Advan. Phys. 6, 418 (1957).

19. D. Porter and A. H. Heuer, J. Am. Ceram. Soc. 60, 182 (1977).

20. R. W. Rice, "Fracture Mechanics of Ceramics," R. C. Bradt, D. P. H. Hasselman and F. F. Lange, eds., Plenum, New York (1974), vol. 1, p. 323.

21. J. E. Blendell, R. L. Coble and R. J. Charles, "Ceramics Microstructure '76," R. W. Fulrath and J. A. Pask, eds., Westview Press, Boulder (1977).

22. W. Boas and R. W. K. Honeycombe, Proc. R. Soc. (A) 186, 57 (1946).

23. A. G. Evans and D. R. Clarke, "Thermal Stresses in Severe Environments" (1980), D. P. H. Hasselman and R. A. Heller, eds. Plenum Publishing Co., New York.

24. S. L. Dole, O. Hunter, Jr., F. W. Calderwood and D. J. Bray, J. Am. Ceram. Soc. 61, 486 (1978).

Table 1.

		Al_2O_3	$MgTiO_5$	H_2O
E (GPa)		420	240	240
ν		0.2	0.2	0.2
$\Delta\alpha$ ($\times 10^{-6}/^{\circ}K$)		0.37	5	5
ΔT ($^{\circ}K$)		1600	1000	1000–1600
$\gamma_{g.b.}$ (Jm^{-2})		3	1 5	1.5
c (μm)	prediction by Eq. 4.10	63	0.5 2.6	0.8 0.3
	prediction by Eq. 4.11	75	0.6 3.1	0.9 0.4
	observed	80(1)	3(2)	2(24)

Figure Captions

Fig. 1. Schematic figure of the stress field of a concentrated force in an infinite body.

Fig. 2. Schematics of cracks in symmetrical and non-symmetrical stress fields.

Fig. 3. TEM micrograph of microcracks in a ZrO_2 grain after martensitic transformation.[+]

Fig. 4. Schematics of one twin pair in a homogeneous matrix.

Fig. 5. Plot of normalized normal stresses along the twin terminating interface versus distance from corner for two and six twin structures.

Fig. 6. Plot of normalized stress intensity factor versus normalized crack length for six twin structure.

Fig. 7. Schematics of the crack nature of an edge dislocation and the associated stress intensity factor.

Fig. 8. Schematics of superposition of stress intensity factors of twin field and the edge dislocation.

Fig. 9. Schematics of crack evolution of superpositioned stress intensity factor.

Fig. 10. Plot of stress intensity factors versus crack length for microcracking in ZrO_2.

Fig. 11. Schematic showing of residual stress on grain boundary caused by anisotropic contraction of nearby grains.

Fig. 12. Schematics of surface forces needed to restore the shape of a grain after thermal contraction.

[+]Courtesy of Dr. W. M. Kriven

Fig. 13. A-D Plots of normalized residual stresses along grain boundaries versus distance from corner for four different grain orientation configurations.

Fig. 14. Plot of normalized stress intensity factor versus crack size for a grain boundary crack.

Fig. 15. Schematics of distributed forces on an infinite straight boundary in a body.

Fig. 16. Schematics of the stress field of distributed forces on a finite straight boundary in an infinite body.

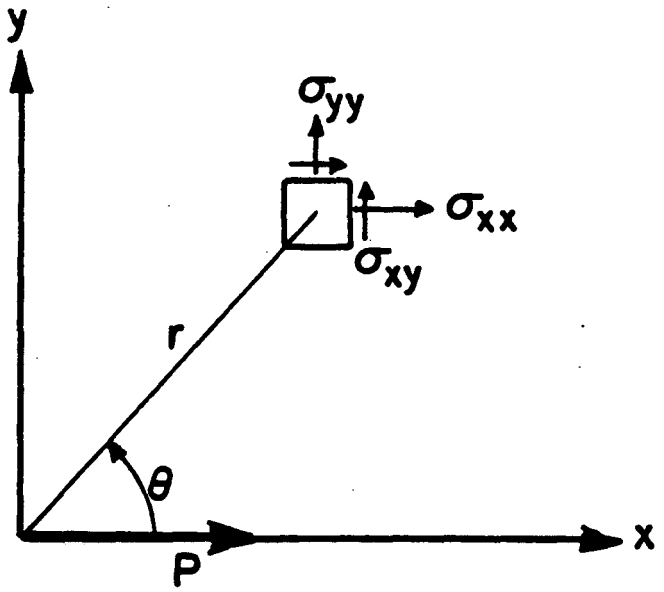

$$\sigma_{xx} = \frac{P}{4\pi}\,\frac{\cos\theta}{r}\left[-(3+\nu)+2(1+\nu)\sin^2\theta\right]$$

$$\sigma_{yy} = \frac{P}{4\pi}\,\frac{\cos\theta}{r}\left[(1-\nu)-2(1+\nu)\sin^2\theta\right]$$

$$\sigma_{xy} = \frac{P}{4\pi}\,\frac{\sin\theta}{r}\left[(1-\nu)+2(1+\nu)\cos^2\theta\right]$$

XBL815-5839

Fig. 1

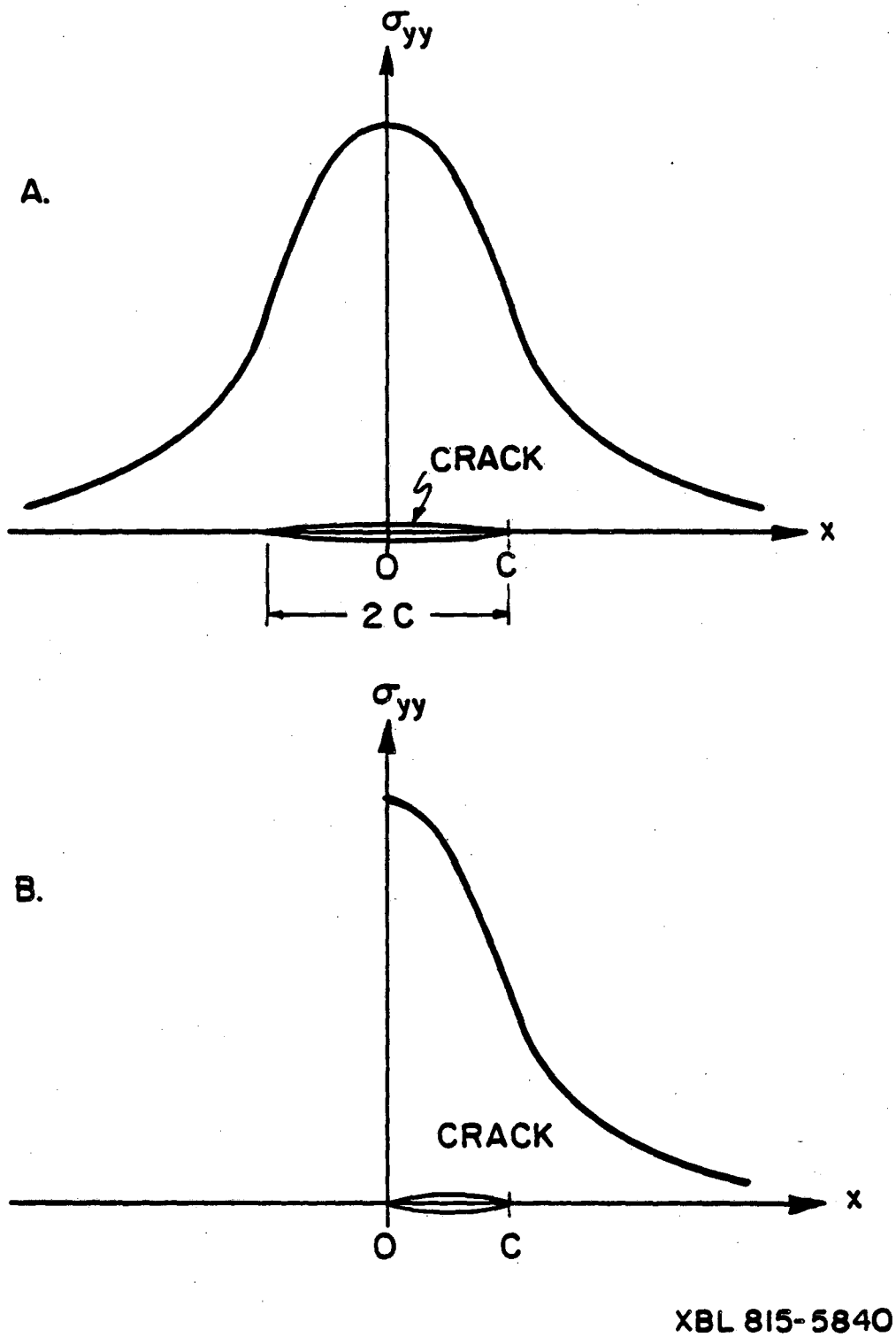

Fig. 2

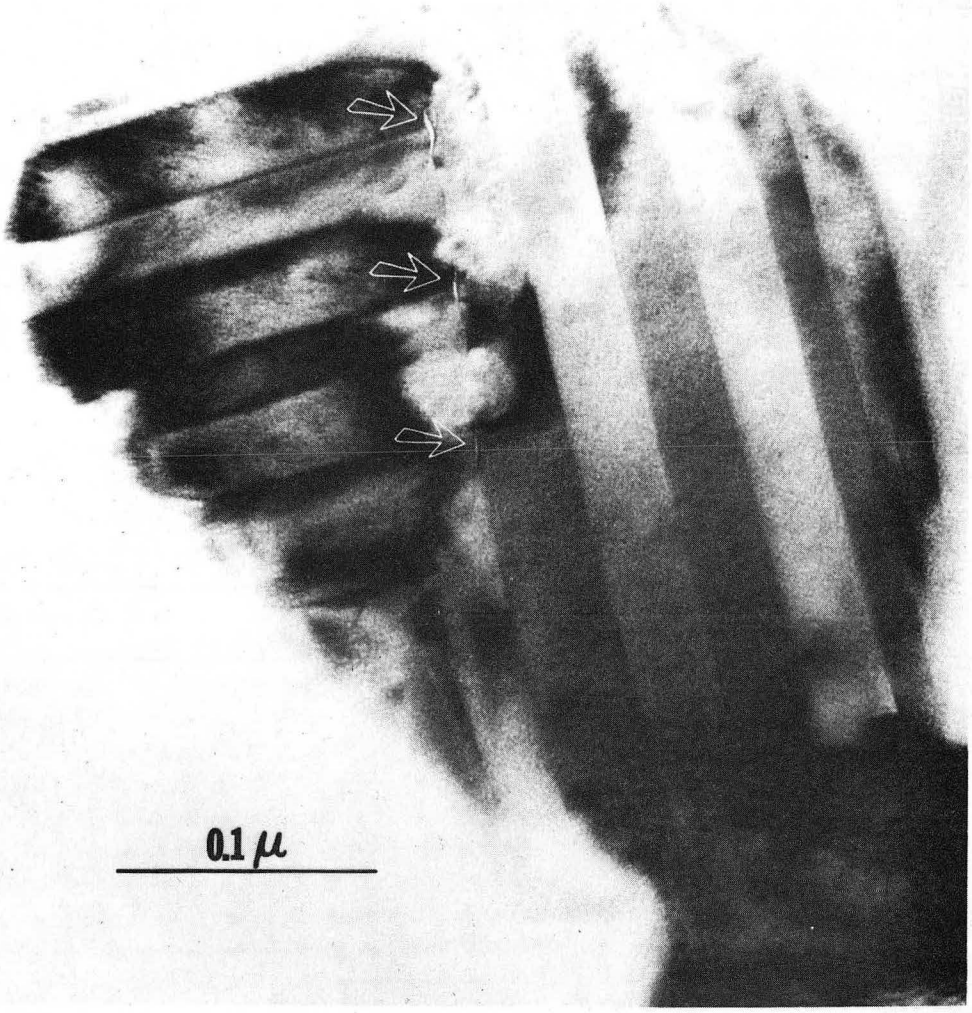

XBB 805-5466

Fig. 3

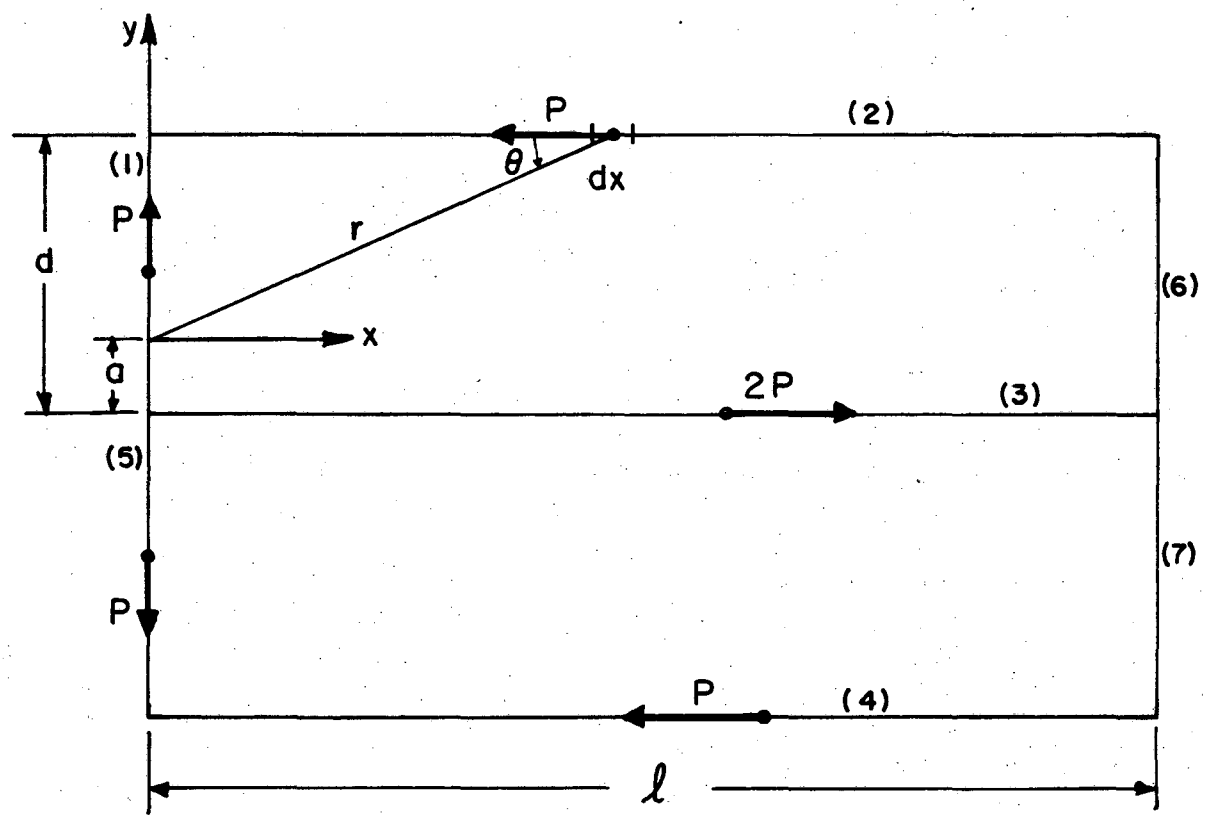

XBL 807-5450

Fig. 4

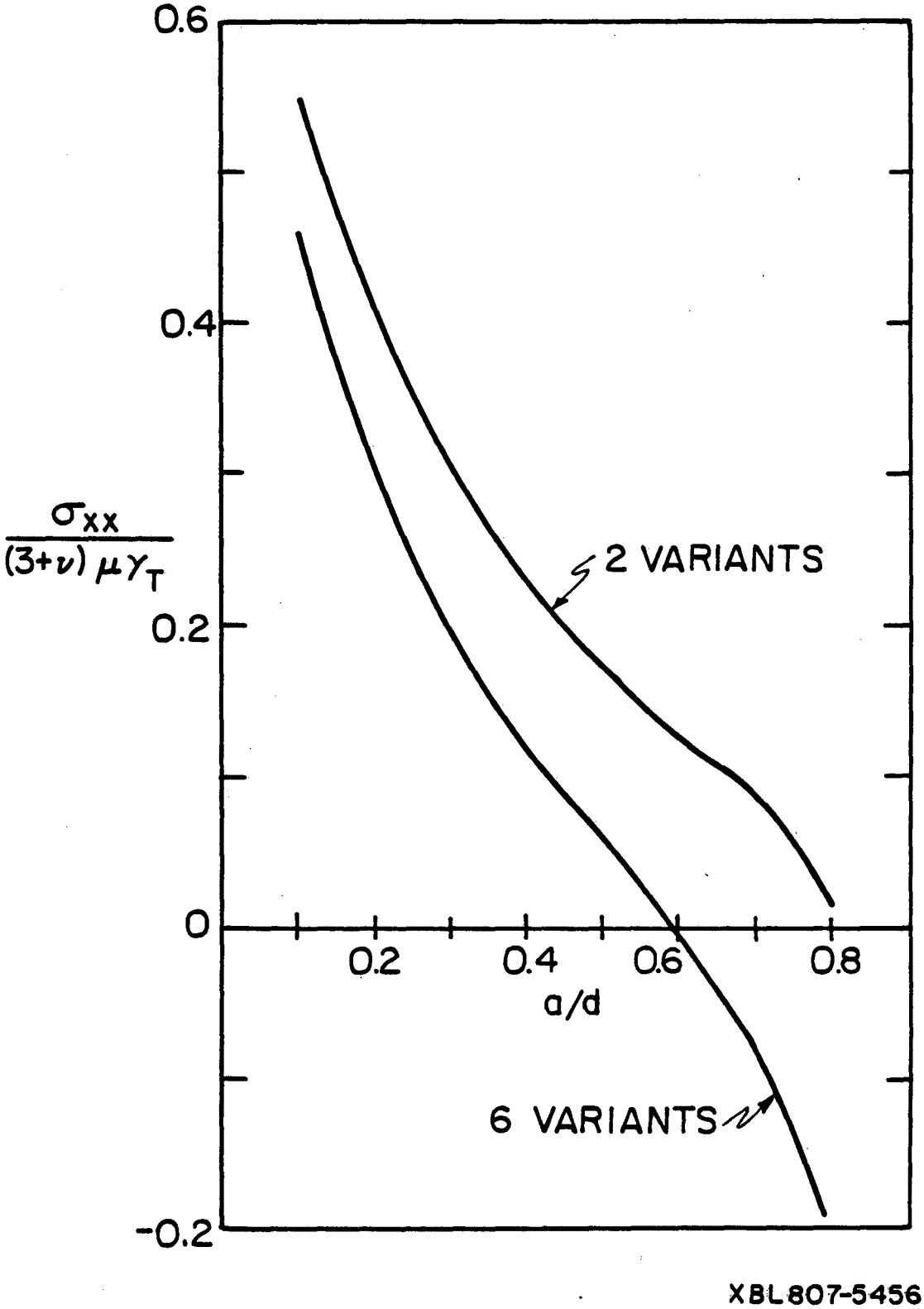
0.6
0.4
0.2
0
-0.2
$\frac{\sigma_{xx}}{(3+\nu)\mu\gamma_T}$
2 VARIANTS
6 VARIANTS
0.2
0.4
0.6
0.8
a/d
XBL807-5456

Fig. 5

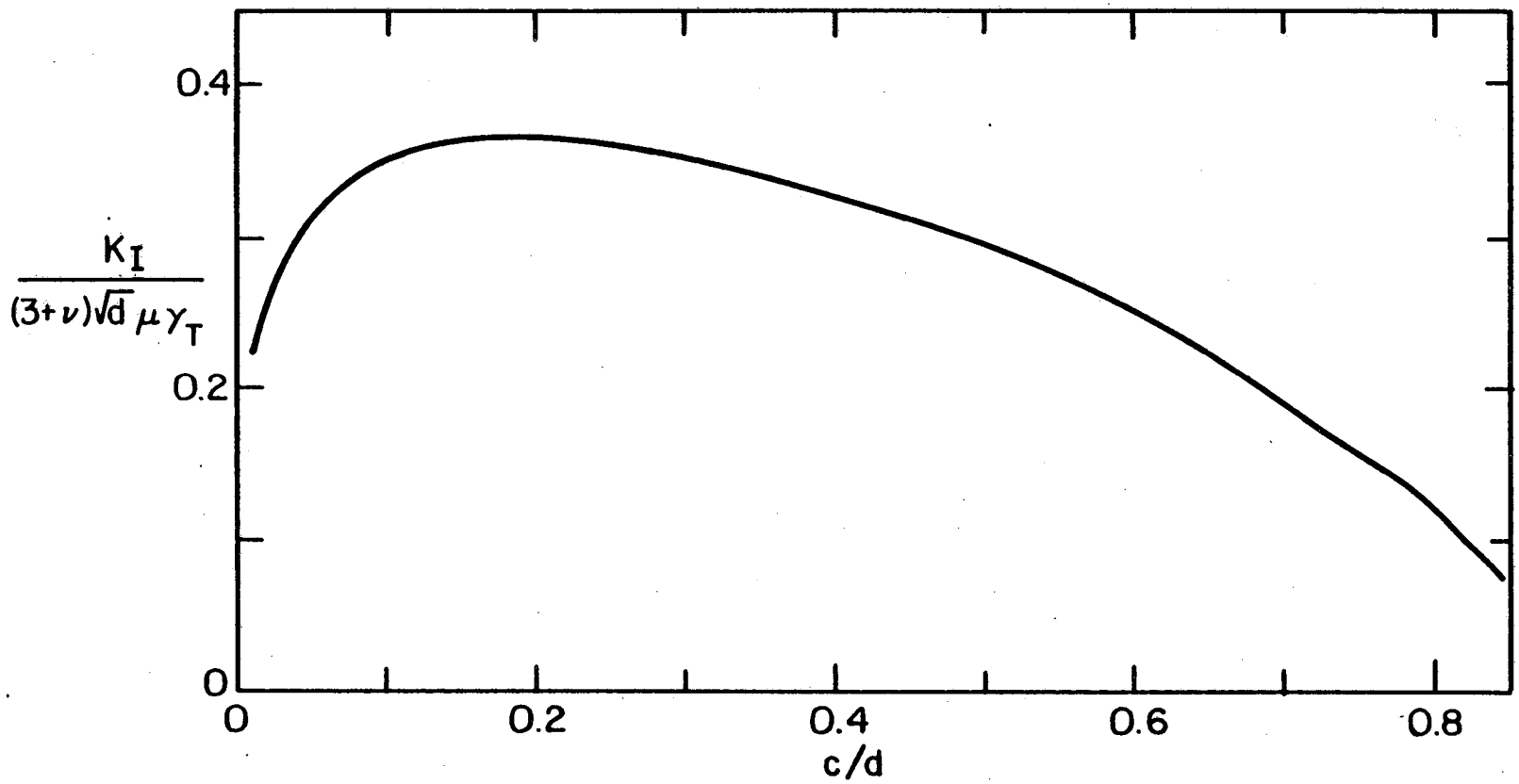

XBL 807-5455

Fig. 6

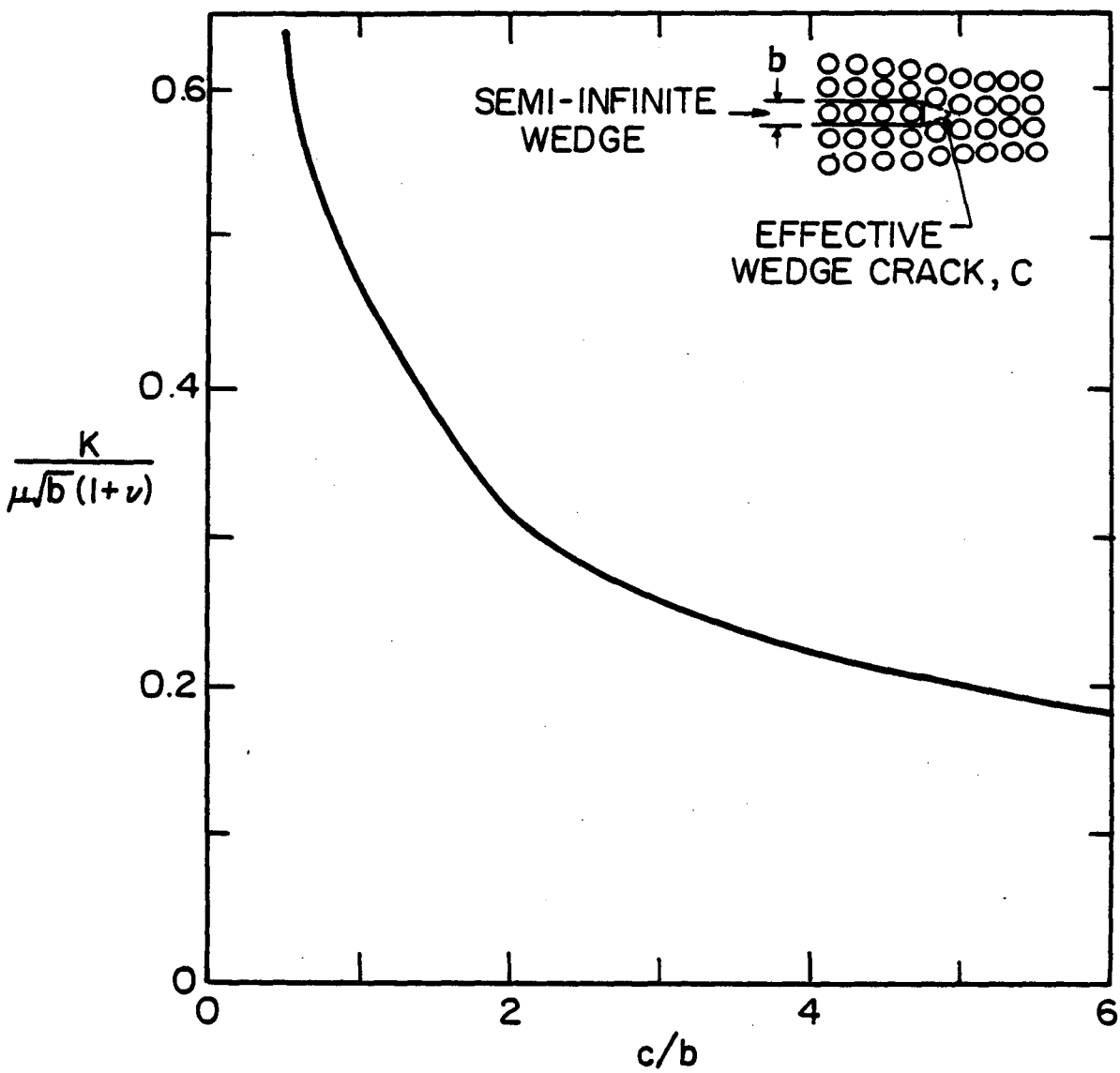

XBL 807-5452

Fig. 7

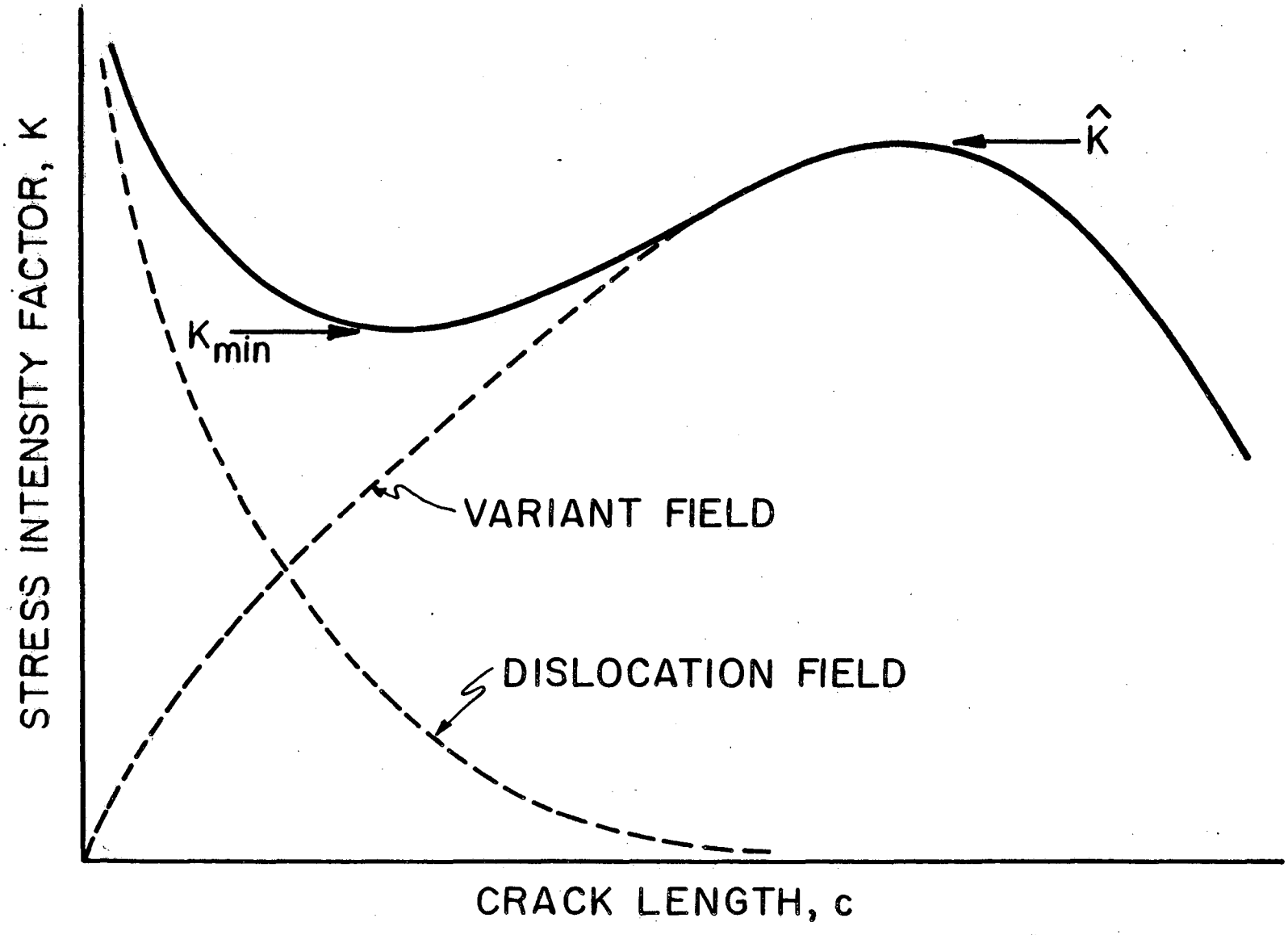

Fig. 8

XBL 807-5464

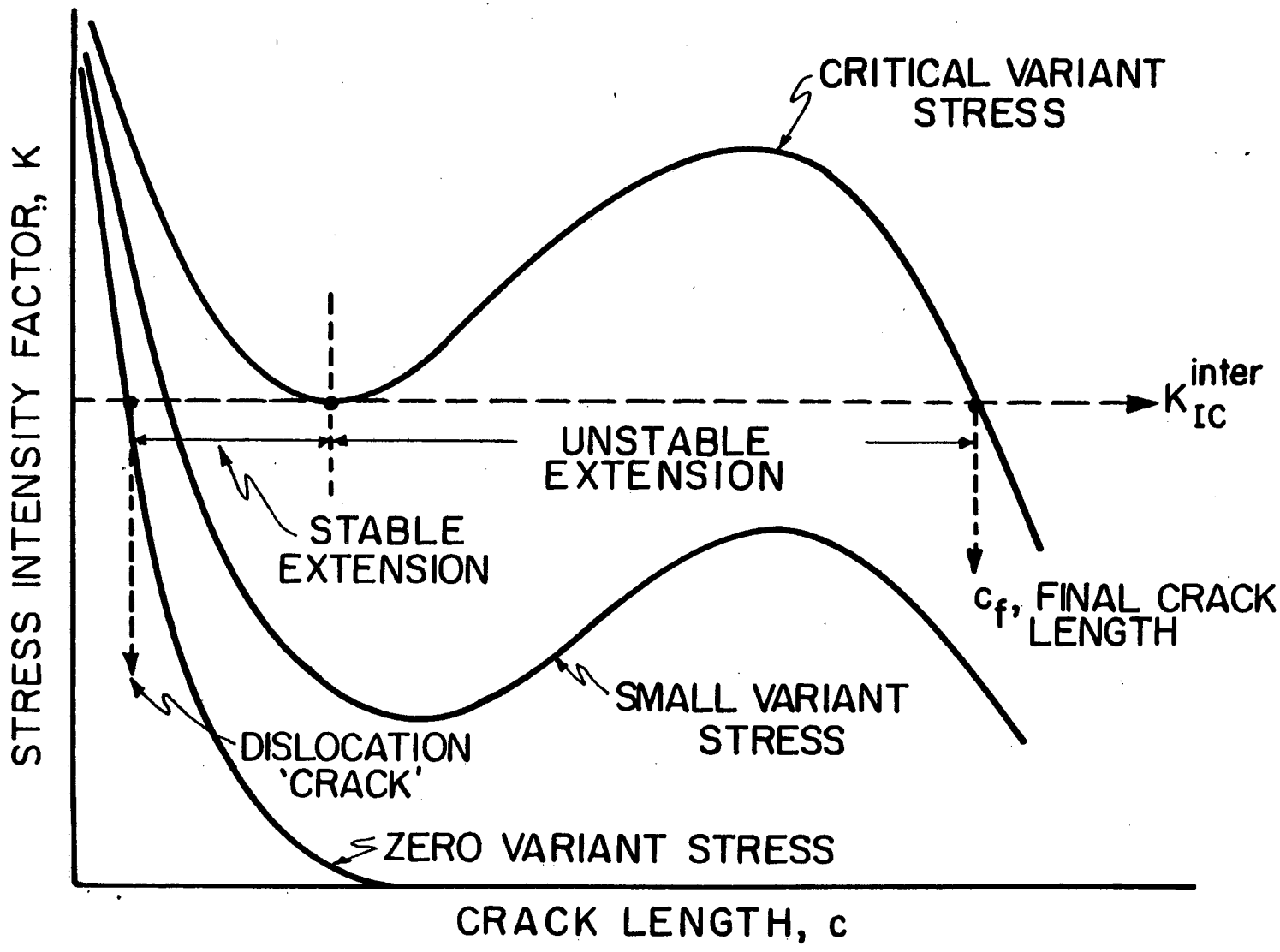

XBL 807-5453

Fig. 9

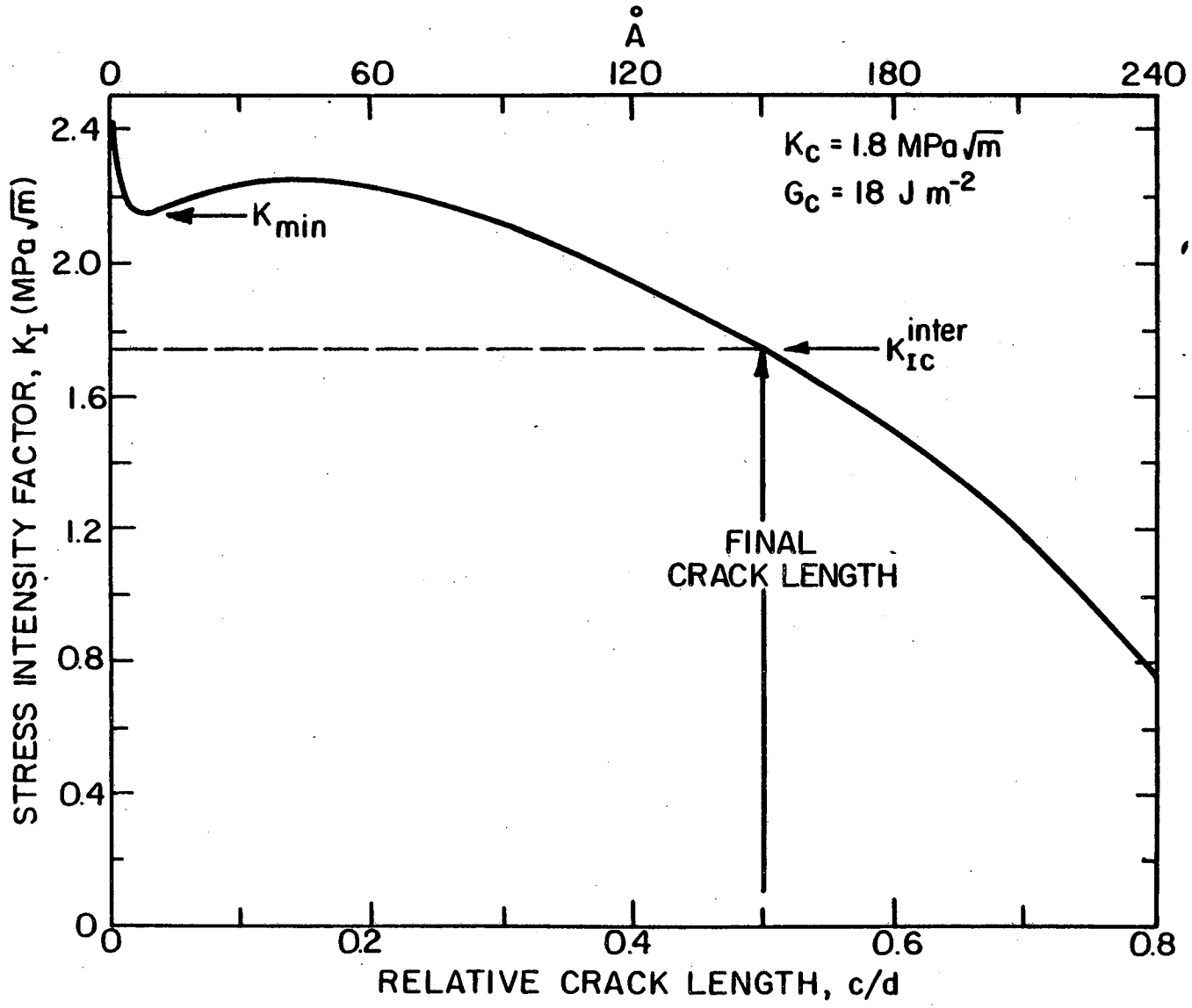

XBL807-5451

Fig. 10

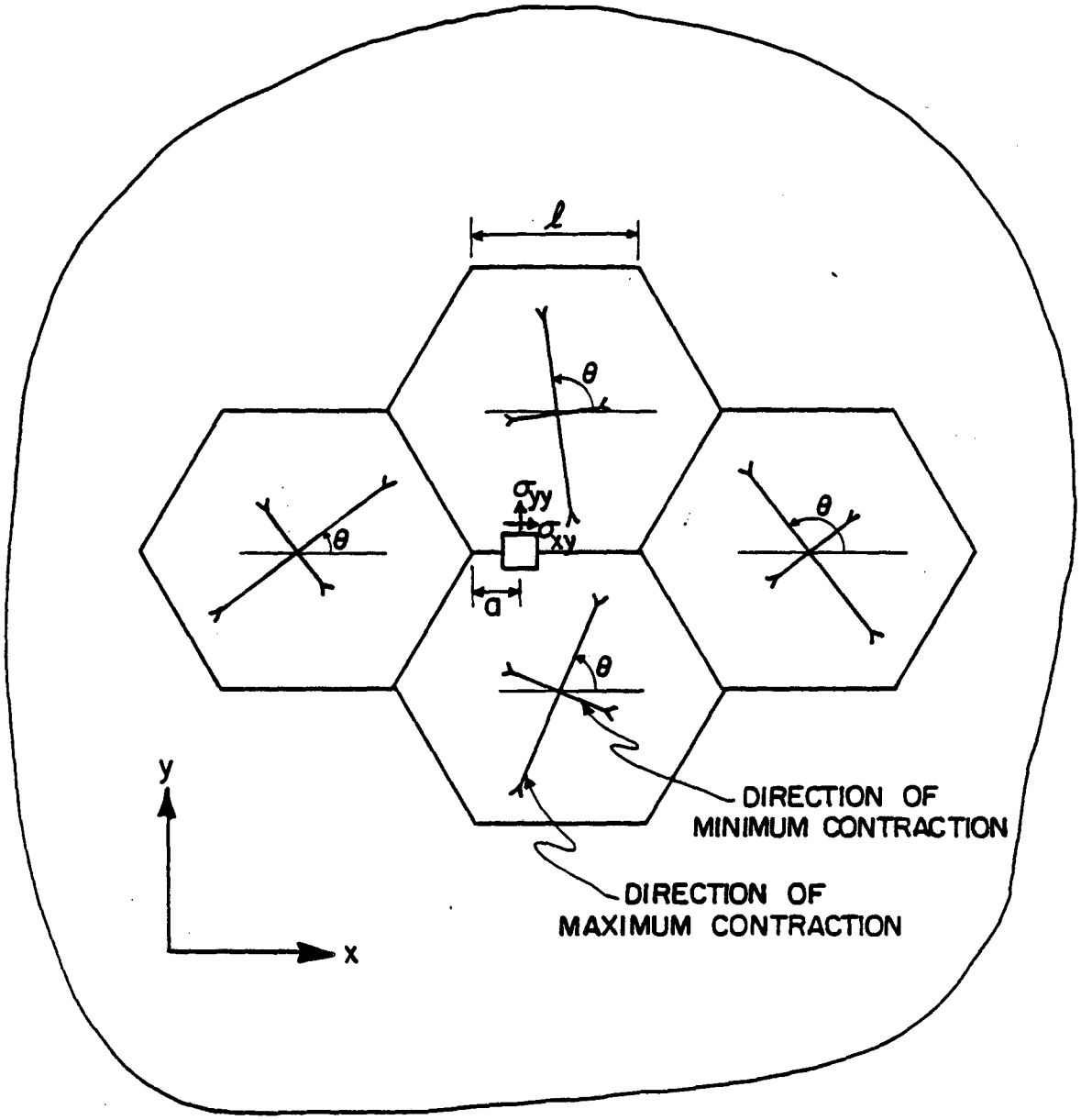

XBL 815-5841

Fig. 11

$$P_x = \sigma_\ell^T \sin\theta\cos\theta - \sigma_s^T \cos\theta\sin\theta$$
$$P_y = \sigma_\ell^T \sin\theta\sin\theta + \sigma_s^T \cos\theta\cos\theta$$

$$P_x = -\sigma_\ell^T \sin(\pi/3-\theta)\cos\theta - \sigma_s^T \cos(\pi/3-\theta)\sin\theta$$
$$P_y = -\sigma_\ell^T \sin(\pi/3-\theta)\sin\theta + \sigma_s^T \cos(\pi/3-\theta)\cos\theta$$

$$P_x = \sigma_\ell^T \sin(2/3\pi-\theta)\cos\theta + \sigma_s^T \cos(2/3\pi-\theta)\sin\theta$$
$$P_y = \sigma_\ell^T \sin(2/3\pi-\theta)\sin\theta - \sigma_s^T \cos(2/3\pi-\theta)\cos\theta$$

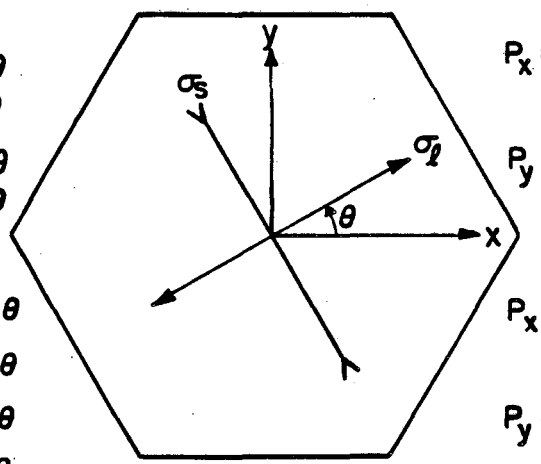

$$P_x = -\sigma_\ell^T \sin(2/3\pi-\theta)\cos\theta - \sigma_s^T \cos(2/3\pi-\theta)\sin\theta$$
$$P_y = -\sigma_\ell^T \sin(2/3\pi-\theta)\sin\theta + \sigma_s^T \cos(2/3\pi\ \ \theta)\cos\theta$$

$$P_x = \sigma_\ell^T \sin(\pi/3-\theta)\cos\theta + \sigma_s^T \cos(\pi/3-\theta)\sin\theta$$
$$P_y = \sigma_\ell^T \sin(\pi/3-\theta)\sin\theta - \sigma_s^T \cos(\pi/3-\theta)\cos\theta$$

$$P_x = -\sigma_\ell^T \sin\theta\cos\theta + \sigma_s^T \cos\theta\sin\theta$$
$$P_y = -\sigma_\ell^T \sin\theta\sin\theta - \sigma_s^T \cos\theta\cos\theta$$

$$\sigma_{xx} = \sigma_\ell^T \cos^2\theta + \sigma_s^T \sin^2\theta$$

$$\sigma_{yy} = \sigma_\ell^T \sin^2\theta + \sigma_s^T \cos^2\theta$$

$$\sigma_{xy} = (\sigma_s^T - \sigma_\ell^T)\sin\theta\cos\theta$$

XBL 815-5842

Fig. 12

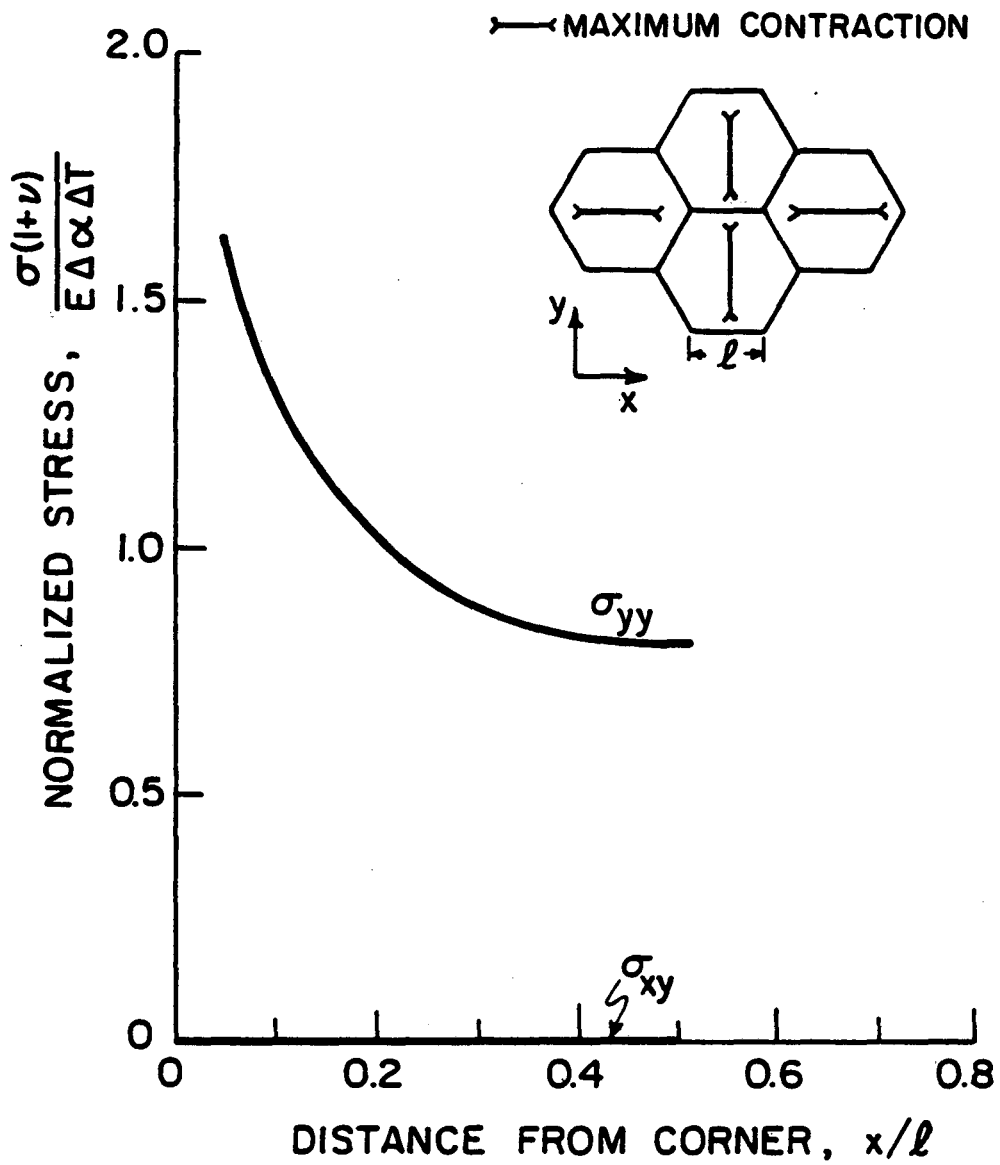

XBL815-5843

Fig. 13.A

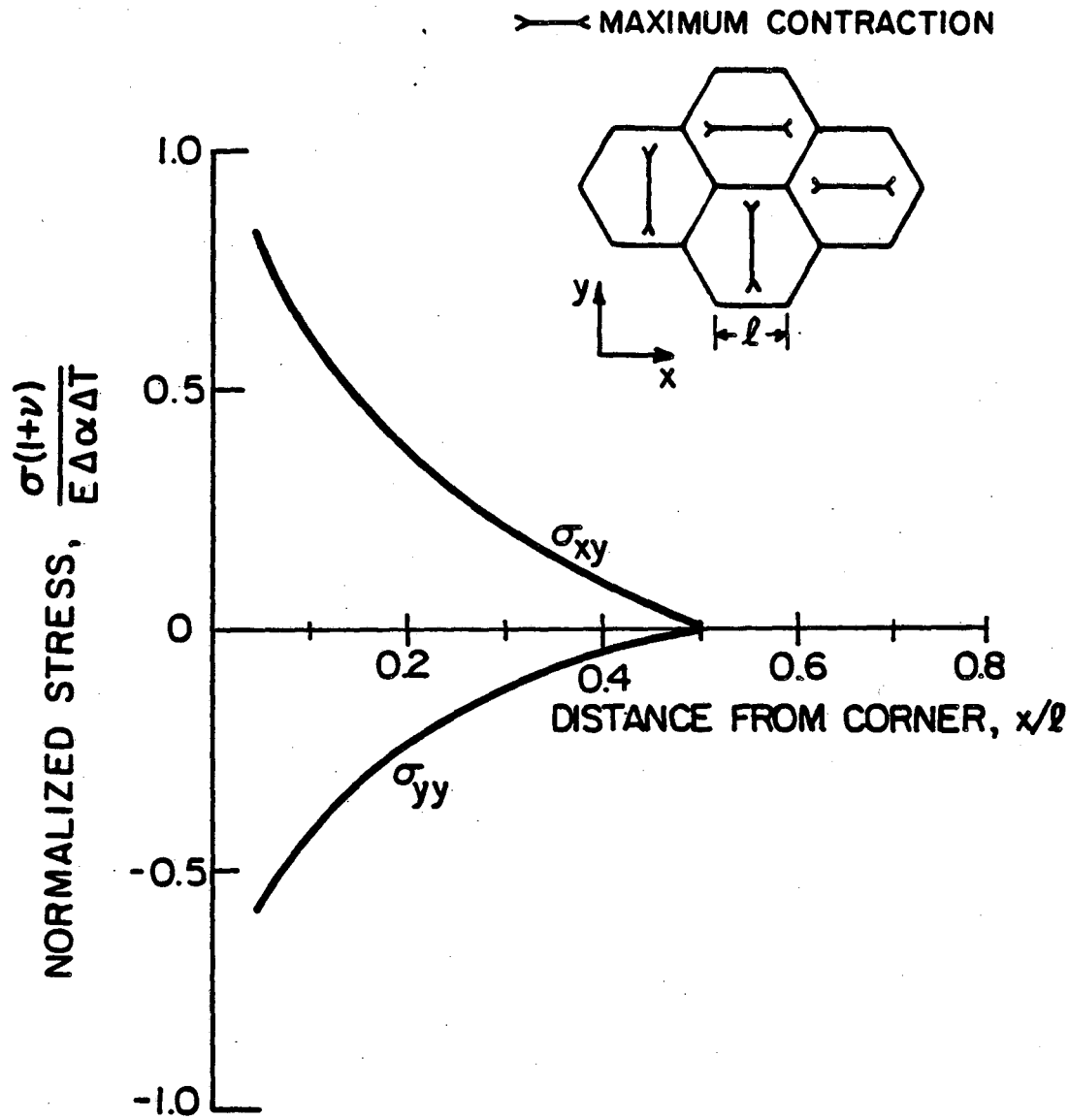

XBL 815-5844

Fig. 13.B

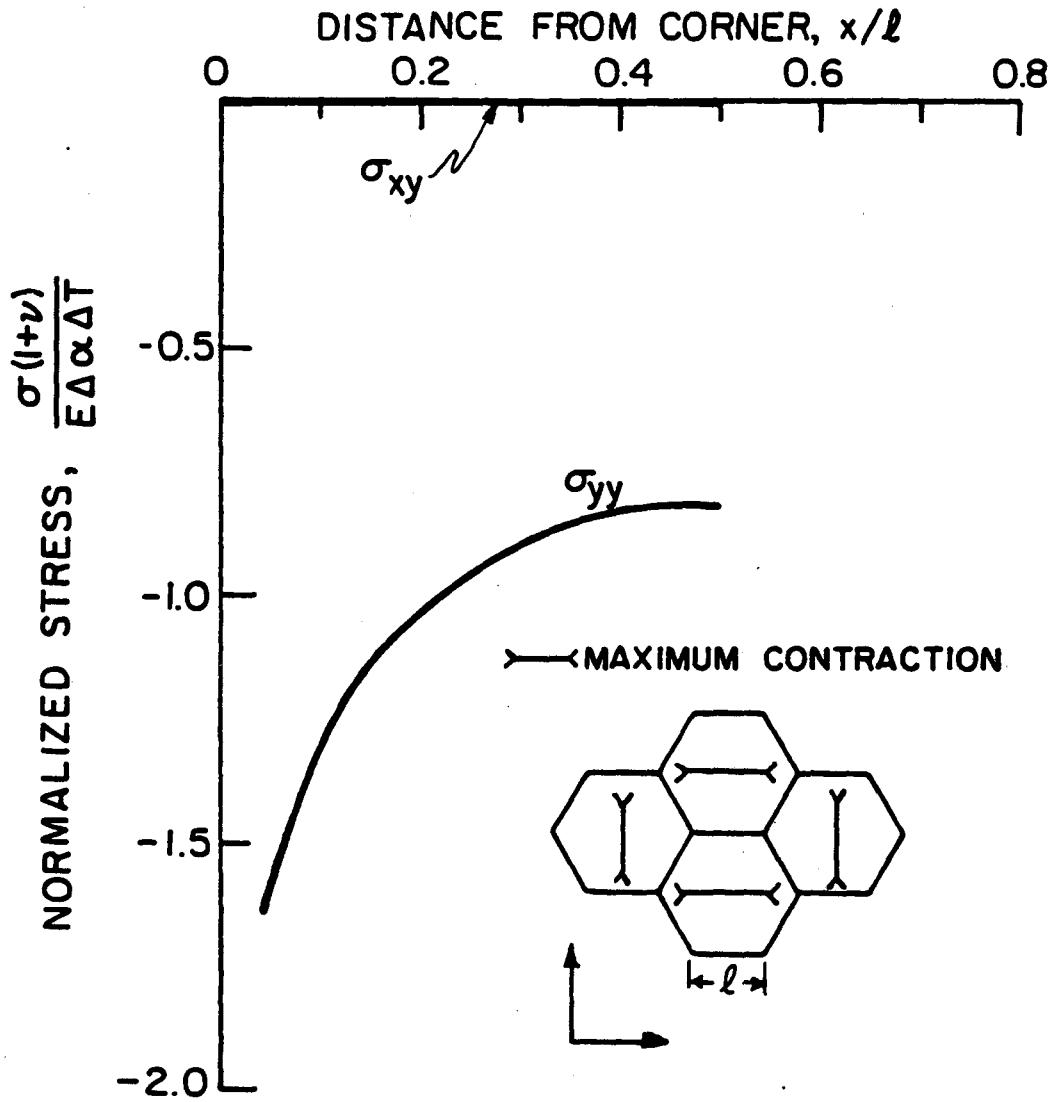

XBL 815-5845

Fig. 13.C

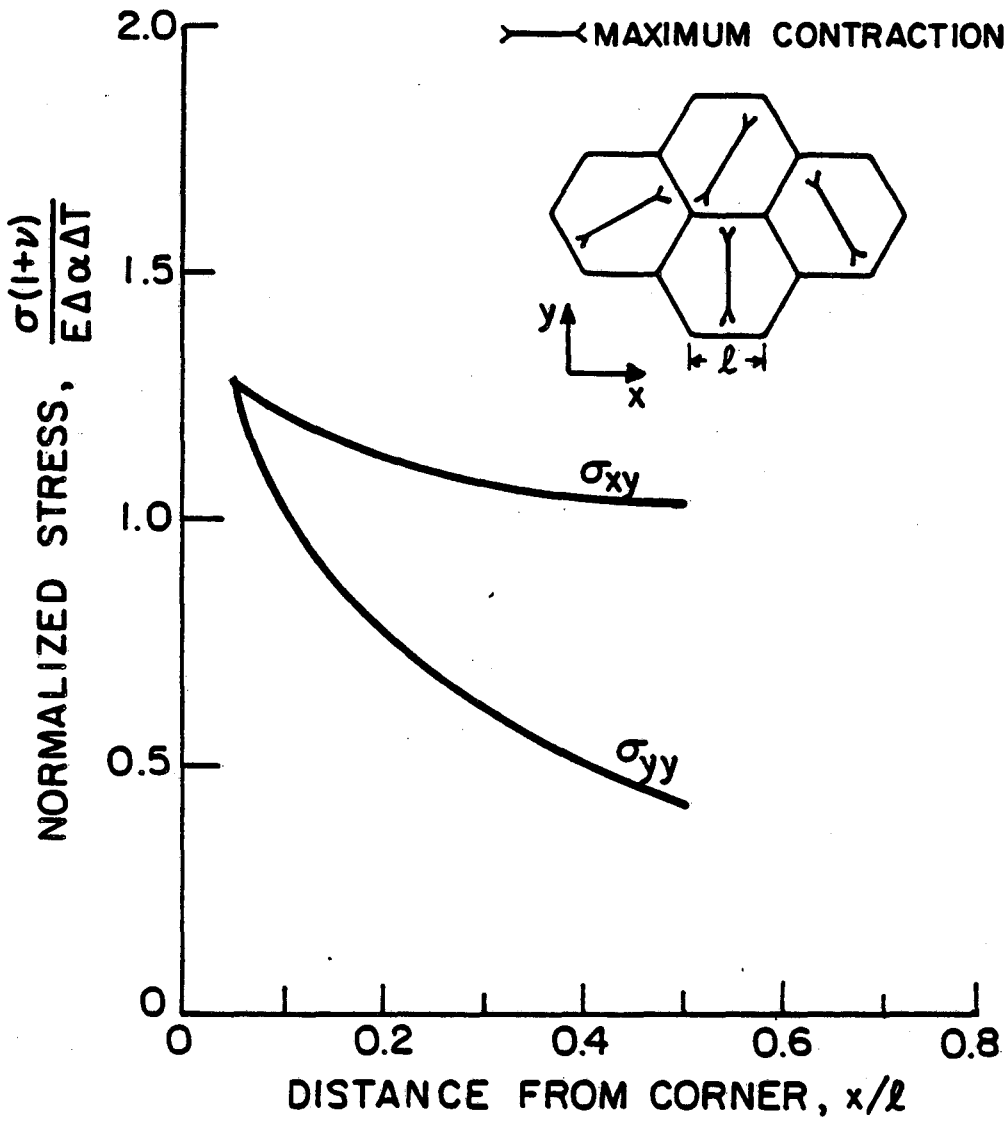

XBL 815-5846

Fig. 13.D

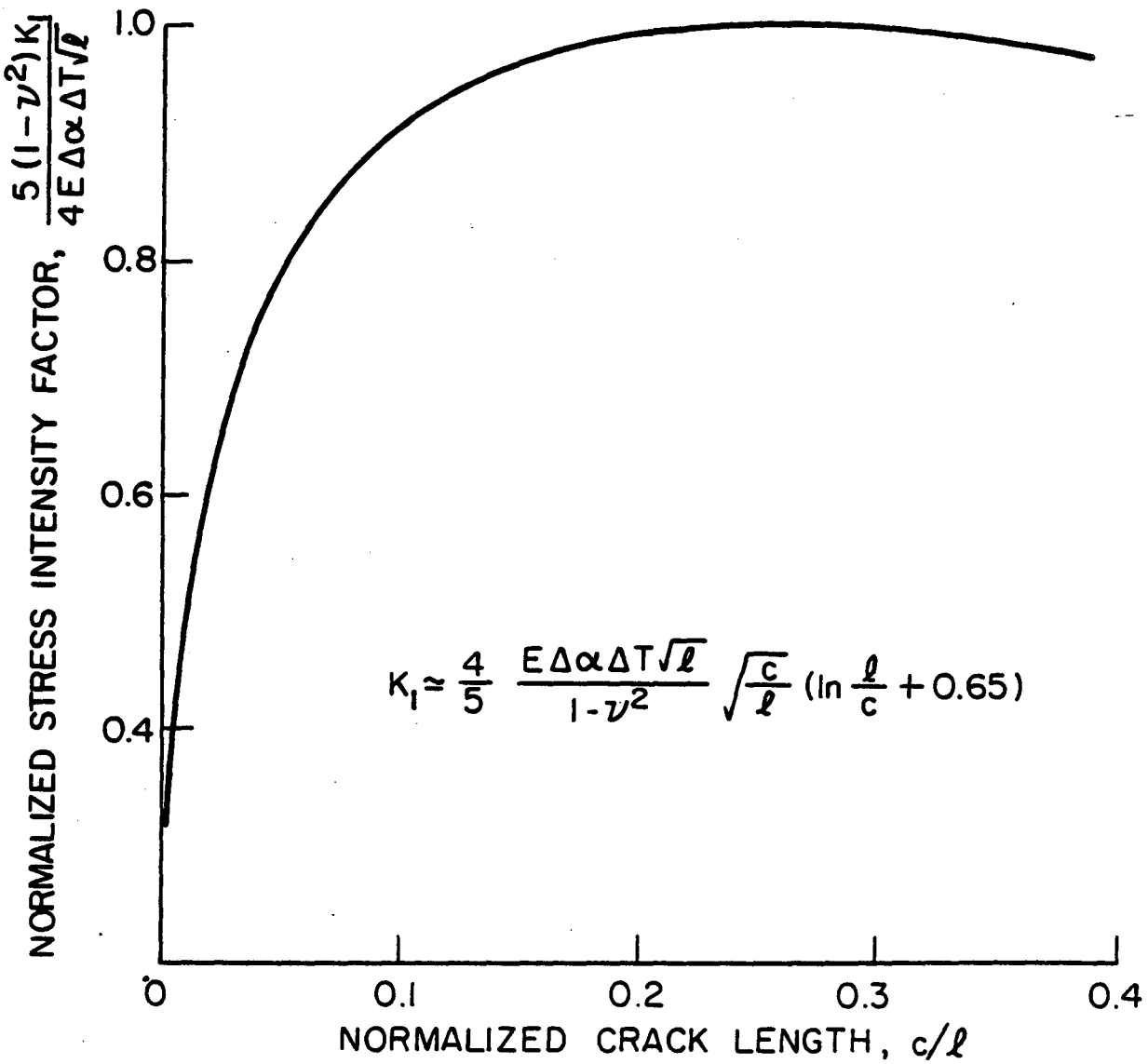

XBL815-5848

Fig. 14

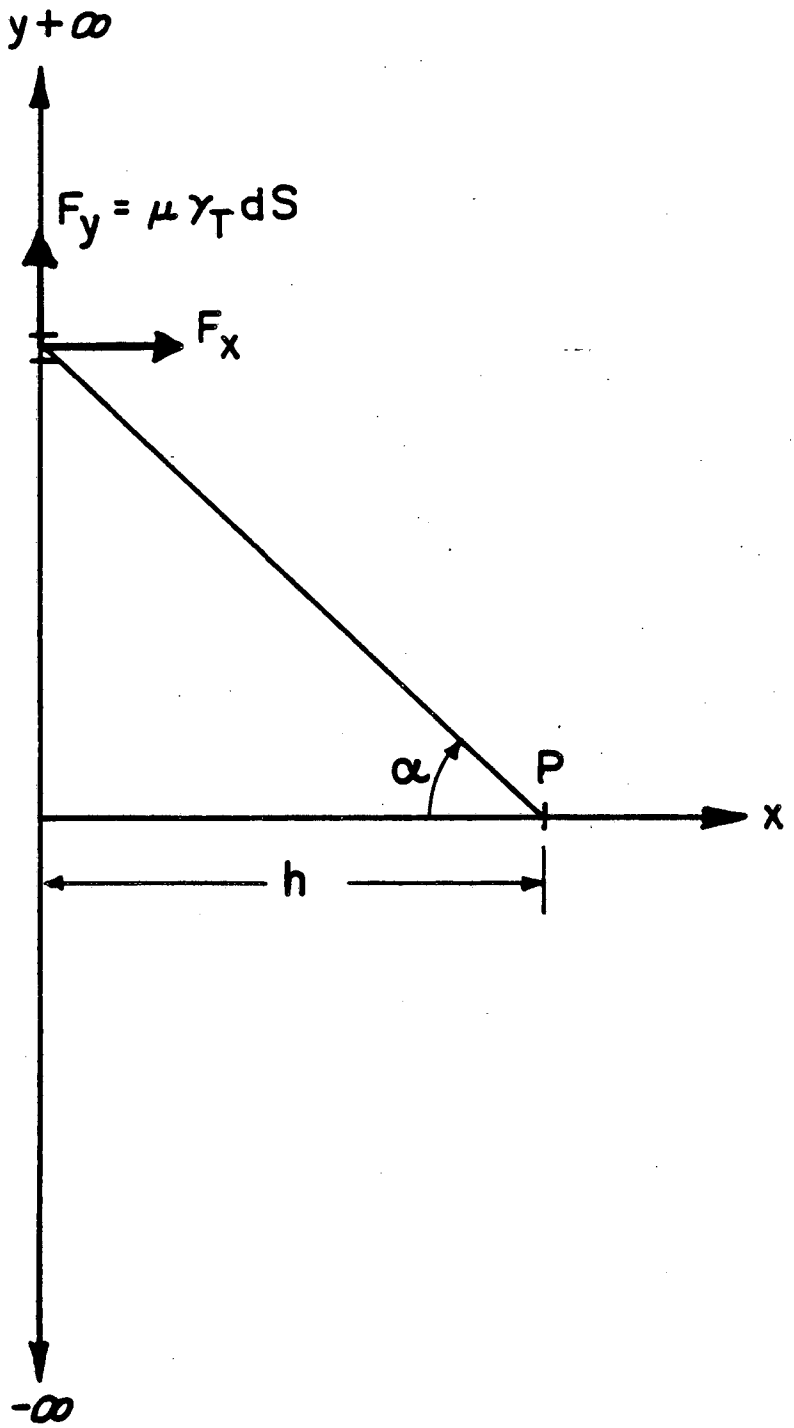

XBL 815-5847

Fig. 15

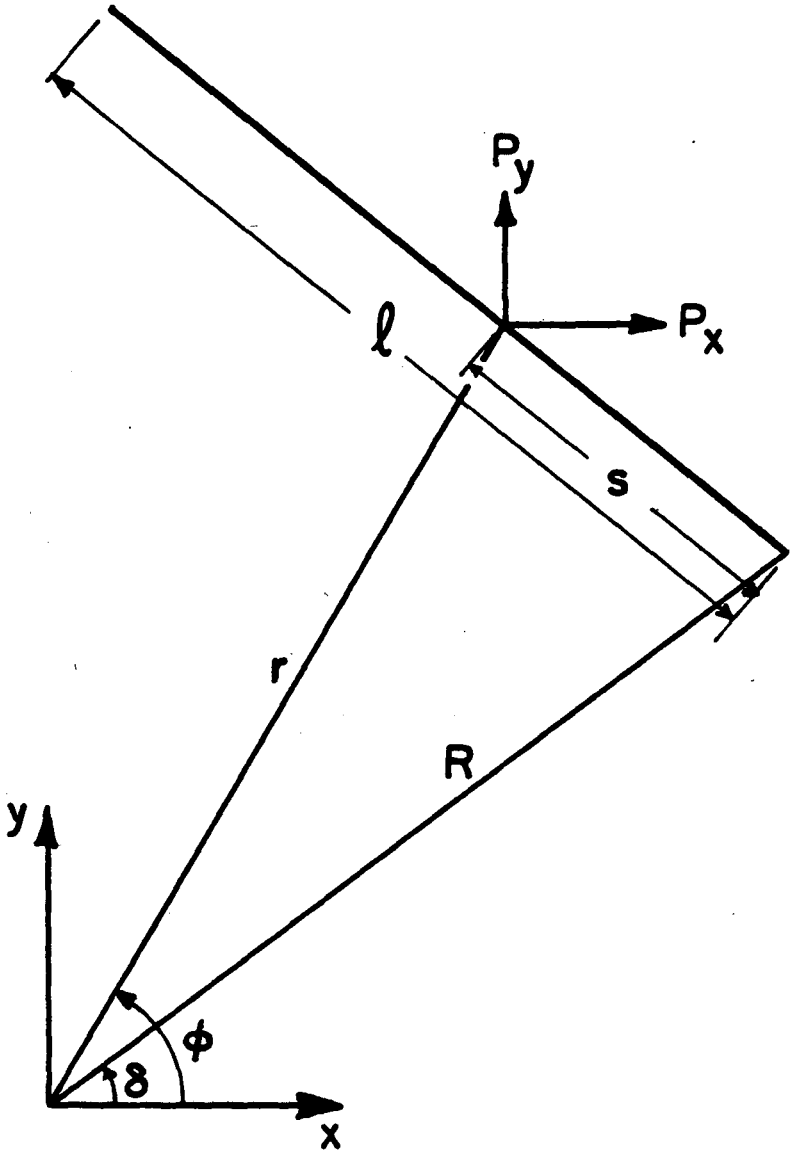

XBL 815-5849

Fig. 16

This report was done with support from the Department of Energy. Any conclusions or opinions expressed in this report represent solely those of the author(s) and not necessarily those of The Regents of the University of California, the Lawrence Berkeley Laboratory or the Department of Energy.

Reference to a company or product name does not imply approval or recommendation of the product by the University of California or the U.S. Department of Energy to the exclusion of others that may be suitable.

TECHNICAL INFORMATION DEPARTMENT
LAWRENCE BERKELEY LABORATORY
UNIVERSITY OF CALIFORNIA
BERKELEY, CALIFORNIA 94720